The natural variability of precipitating clouds over the western Pacific warm pool

By SANDRA E. YUTER* and ROBERT A. HOUZE Jr
University of Washington, USA

SUMMARY

The natural variability of precipitating cloud systems over the western Pacific 'warm pool' is investigated by analysing aircraft C-band radar data collected on 24 aircraft missions during the Coupled Ocean–Atmosphere Response Experiment of the Tropical Ocean and Global Atmosphere programme (TOGA COARE) in relation to the infrared (IR) temperature patterns measured contemporaneously by geosynchronous satellite. The data are analysed at fine (24 km × 24 km) and coarse (240 km diameter) horizontal resolutions, which correspond to typical resolutions of mesoscale and general-circulation models, respectively. The analysis is statistical and imposes no a priori conceptual model or subjectively decided-upon structure categories. The mean IR temperature of cloud tops, and the sizes of rain areas mapped by radar (and objectively subdivided into convective and stratiform sub-areas), are tallied and related to each other to obtain statistics representative of the four-month period of the TOGA COARE.

At fine resolution the precipitation region underlying very cold cloud tops (<208 K) always contained stratiform precipitation and had less than a 50% probability of containing some amount of convective precipitation. The frequency of occurrence of precipitation, the area covered by all types of precipitation, and the area covered by stratiform precipitation all increased with decreasing mean IR temperature. In contrast, the area occupied by convective precipitation was independent of mean IR temperature.

Over a period of sustained convective cell activity, the cells never instantaneously occupied more than a small fraction of the coarse area, and never more than 30% of a fine-grid element. However, as cells weakened they evolved into stratiform precipitation, and the stratiform region grew as each cell finished its active convective phase and was added to the stratiform area. The sustainability of convective cells over time thus determined the overall size of a precipitation area.

Rain-area size did not correlate linearly with mean IR temperature nor any other statistical measure of the IR temperature pattern at coarse resolution. However, two-dimensional joint-probability distributions of mean IR temperature (a measure of cloud structure) and radar echo parameters (which measure precipitation structure) on the coarse scale yield insight into the natural variability of precipitation processes over the warm pool: most notably, large precipitation areas (>50% of a coarse area) tended to have low mean cloud-top temperatures (<235 K), and high mean cloud-top temperatures (>235 K) were associated with small precipitation areas (<50% of a coarse area). However, the converse of these two results was not true. Low mean cloud-top temperatures (<235 K) were associated with a wide range of precipitation areas from near 0 to 90% of a coarse area, and small precipitation areas (<20% of a coarse area) had mean IR temperatures ranging from 210–295 K.

Once precipitation regions reached a large enough size (near 20% of a coarse area), the cloud systems were efficient at spreading ice outside of the boundaries of the precipitation regions. Larger rain areas (>20% of a coarse area) were predominantly stratiform (>75% by area and >50% by rainfall amount). Precipitating cold clouds (containing ice) with stratiform area fractions <50% were not observed.

During active phases of the intraseasonal oscillation (ISO), the probability that there were no satellite-observable clouds within a coarse-resolution area of the aircraft sample was practically zero (maximum mean IR temperature never >286 K), while during suppressed phases the near or total absence of clouds was common. Large rain areas with very cold cloud tops were common under active conditions but not under suppressed conditions. The large rain areas with very cold cloud tops (>20% of the coarse area and <235 K mean IR temperature) occurred primarily during the active phase and were 75–100% stratiform by area and >70% by rain fraction. In the suppressed phases, stratiform rain fractions varied widely since most of the rainfall was associated with small precipitation areas.

Although the joint-probability distributions differ substantially between active and suppressed phases of the ISO, the overall precipitation-area size is not strongly related to wind speed, wind direction, or thermodynamic variables, as seen in the storm inflow soundings obtained by the TOGA COARE aircraft.

KEYWORDS: Airborne observations   Rainfall   TOGA COARE   Tropical meteorology

1. INTRODUCTION

A specific goal of the Tropical Ocean and Global Atmosphere Coupled Ocean–Atmosphere Response Experiment (TOGA COARE) was 'to describe and understand the

* Corresponding author: Department of Atmospheric Sciences, Box 351640, University of Washington, Seattle, Washington 98195, USA.
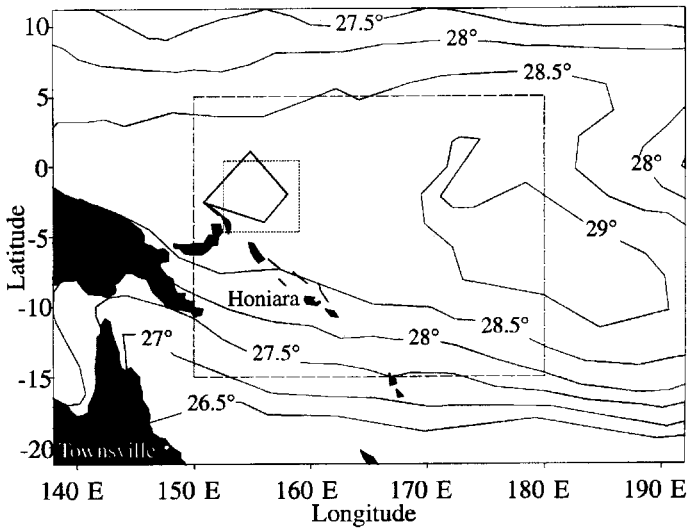
Figure 1. Map of the TOGA COARE region. Locations of the turboprop aircraft base, (Honiara, Guadalcanal, Solomon Islands) and the jet aircraft base (Townsville, Australia) are indicated. The quadrilateral centred near 2°S, 156°E is the intensive flux array. The dotted box is the region covered by the shipborne C-band radars on board the R.V. *Vickers* and PRC #5. The dashed box is the warm pool region used for the statistics in Fig. 2. Contours of mean intensive observing period sea surface temperature (SST, °C) indicate the location of the warm pool. (Time-averaged NMC SST global analysis provided by Shuyi Chen.)

principal processes that organize atmospheric convection in the western Pacific warm pool region' (Webster and Lukas 1992). The nature of convective activity over the warm pool region (Fig. 1) is variable, comprising a spectrum of clouds, including isolated shallow cumulus, deep giant cloud clusters, and long-lived groups of cloud clusters called 'super clusters' (Nakazawa 1988, 1995; Mapes and Houze 1993; Chen *et al.* 1996). Climatologically, over the tropical oceans, the smaller clouds occur much more frequently than the large clusters. The small clouds may rain heavily locally, but the larger systems dominate total rainfall and cold cloud-top coverage.

Numerical studies have shown that large-scale tropical dynamics are sensitive not only to the amount and distribution of precipitation, but also to the *precipitation structure*—especially to the amounts and distribution of convective versus stratiform precipitation (Raymond 1994; Mapes and Houze 1995; Mapes 1997). Thus, the range of the natural variation of tropical precipitation structure is vital information in unravelling the complicated feedbacks between convective activity and large-scale dynamics.

Over a four-month time period it is difficult, if not impossible, to obtain a truly representative climatological sample. With this constraint in mind, the TOGA COARE turboprop aircraft programme was designed such that during the intensive observing period (IOP), the mobility of airborne radars was utilized to obtain a roughly equal distribution of flight hours in all portions of the cloud spectrum within the TOGA COARE domain (Fig. 1) (Yuter *et al.* 1995c). As an aircraft flies through a region of convective activity, the data it collects form a series of snapshots of the storm system, showing different regions in different stages of development. The population of these snapshots of precipitation structure and coincident infrared (IR) temperature is the foundation of our study. The shipborne radars (Short *et al.* personal communication), located in the eastern portion of the intensive flux array (IFA) (Fig. 1), captured an Eulerian sample of cloudiness over roughly a 400 km × 300 km area with roughly similar relative frequency characteristics
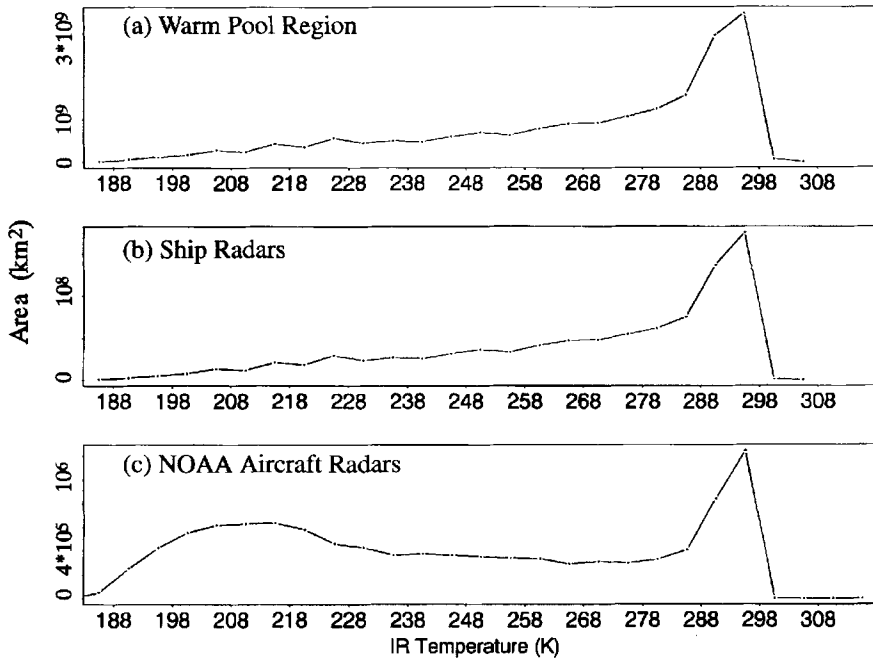
Figure 2.   Histograms of the cloud-top infrared (IR) temperature for (a) the warm pool region (dashed box in Fig. 1), (b) the TOGA COARE shipborne radar region (dotted box in Fig. 1), and (c) the sampling by NOAA WP-3D aircraft during the TOGA COARE. Histogram bin size is 5 K.

to the more climatological spectrum obtained over the entire warm pool region during the four months of the TOGA COARE (Figs. 2(a) and (b)). In comparison with their relative climatological frequency, the aircraft radars oversampled the infrequently occurring large colder cloud systems (Fig. 2(c)), and thus obtained a larger sample of large very cold clouds than did the shipborne radars. Our approach is to utilize the more even distribution of samples within the cloud spectrum of aircraft radar data, rather than the shipborne radar data, to bound the characteristics of naturally occurring clouds over the warm pool. The criteria for representativeness is thus one of obtaining sufficient samples within each segment of cloud spectrum to characterize the approximate range of conditions.

The possible states of a chaotic dynamical system such as the atmosphere are limited (Lorenz 1993). In the absence of an exact numerical description of a phenomenon, information on the possible states of a nonlinear dynamical system can be reconstructed using experimentally accessible quantities (Packard *et al.* 1980; Froehling *et al.* 1981; Abarbanel *et al.* 1993). To describe the possible states of tropical precipitating clouds over the warm pool, we analyse the radar-observed precipitation structure seen in cloud areas defined by satellite-observed IR temperature patterns. More specifically, we examine joint-probability distributions of aircraft radar and satellite data obtained during the TOGA COARE (1 November 1992–28 February 1993). Joint-probability distributions of well-selected empirical variables reveal characteristics of the natural variability in terms of the physically feasible combinations of variables, similar to the way a phase space attractor describes the physically feasible combinations of variables in a nonlinear dynamical system.

To refine the analysis of the radar data, we use an objective method to identify precipitating pixels in airborne radar reflectivity data and classify them as convective or stratiform.

The classified radar data are mapped onto hourly IR images from the Japanese Geosynchronous Meteorological Satellite (GMS). The GMS IR data are the only data set that had continuous coverage over the entire TOGA COARE domain at time and spatial scales commensurate with the aircraft radar data. The satellite data define the cloud structure, while the radar data identify the precipitation structure. Data from *all* TOGA COARE aircraft missions where both GMS IR and airborne C-band reflectivity data were available are included in this analysis[*].

To make the results of this study relevant to numerical modelling, we analyse the precipitation structure and IR temperature characteristics at two scales: a fine scale (24 km × 24 km) similar to grid sizes in mesoscale models, and a coarse scale (240 km in diameter) similar to grid sizes in general-circulation models (GCMs). Basic characteristics of the local environment of the storm derived from 12-hourly synoptic data and storm inflow soundings are also examined to determine how the environmental conditions external to the precipitating cloud systems affect the distribution of the cloud-system variables.

The objective of this study is to examine the relationships between observations made during the TOGA COARE of nearly simultaneous cloud-top temperature and precipitation structure to answer the following questions: On a fine-grid scale (24 km × 24 km), what is the association of precipitation structure and overlying average IR temperature? On a coarse-area scale (240 km diameter), what are the joint-probability distributions of the precipitating cloud system in terms of mean IR temperature, precipitation area, and stratiform fraction of the area and amount of rainfall? What is the manifestation of the external environmental conditions on the joint-probability distributions? This information will aid in understanding the processes that organize convection by documenting a set of possible naturally occurring states, and providing validation information for precipitation characteristics derived from satellite-based sensors, forecast models, and theoretical studies.

2. DATA AND METHODOLOGY

(a) GMS IR data

The Visible and Infrared Spin-Scan Radiometer (VISSR) on board the GMS satellite begins its hourly scanning sequence between 25–30 min after the hour and takes ~30 min to complete scanning the full-earth disk (Meteorological Satellite Center 1989). The VISSR scans individual 140 μrad wide lines from west to east starting at 90°N latitude and ending at 90°S latitude. Thus, the IR sensor scans the equatorial region each hour between 40–45 min after the hour. The IR data resolution is ~5 km × 5 km at the sub-satellite point at 0°,140°E.

The limitations of the IR sensor constrain the interpretation of IR temperature in terms of cloud-top temperature. Clouds that are smaller than the footprint of the sensor (~5 km × 5 km at 0°,140°E and slightly larger over the TOGA COARE region) will be averaged with the radiance received from the surrounding ocean areas, yielding an IR temperature higher than the actual black-body temperature of the cloud tops (the 'beam-filling' problem). Similarly, in the case of broken clouds, where the cloud shield contains cracks of clear air smaller than the sensor footprint, the resulting IR temperature will also be higher than that corresponding to an unbroken cloud shield at the same altitude. The joint distribution of visible reflectance and IR temperature distribution in clouds over the western Pacific indicates that clouds characterized by IR temperatures <220 K have reflectances

---

[*] Data are used from all P-3 missions except from the mission on 11 January 1993. The GMS satellite underwent maintenance on that day and no satellite data were available.

>0.7 and thus have significant optical depths (Fu *et al.* 1990). Higher IR temperatures may or may not correspond to optically thick clouds (Fu *et al.* 1990). Optically thin clouds (not absorbing and radiating as black bodies) indicate a temperature higher than that of an optically thick cloud at the same cloud-top altitude because the radiometer will sense radiation from lower (higher temperature) levels combined with the radiation from cloud top. These factors hamper the distinction in IR data between *cold clouds* which extend above the 0 °C level and thus contain ice, and *warm clouds* which do not extend above the 0 °C level and do not contain ice (Wallace and Hobbs 1977). In this study we do not keep track of the characteristics of contiguous areas of cloudiness over multiple grid elements, and thus we cannot distinguish between true warm clouds and the warmer parts of cold clouds. The definition of warm clouds is distinct from that of *warm rain*. Warm-rain processes—primarily coalescence of drops—are active below the 0 °C level in *both* warm and cold clouds.

The distribution of IR temperatures observed by the GMS satellite over the TOGA COARE domain during the four months of the experiment is strongly skewed toward higher temperatures, which is indicative of the low frequency of large storms (Fig. 2(a)). The observed peak in IR temperature is at 293–298 K which is several degrees lower than the sea surface temperatures in the region (300.5–302.5 K). This several degree temperature difference between the measured brightness temperature for clear-sky conditions and the black-body temperature of the ocean surface may be ascribed to water vapour continuum absorption (Roberts *et al.* 1976) and reflectance from atmospheric aerosols (Stephens 1994) within the 10.5–12.5 μm channel on the VISSR infrared sensor. In addition, it is rare for small fair weather cumulus to be entirely absent over the warm pool. Thus, even in ostensibly clear weather, small fair weather cumulus will also lower the mean IR temperature sensed by the satellite compared with the black-body temperature of the ocean surface.

Some of the hourly IR data images were entirely missing. Regions of bad data within an image were either set to a bad-data flag value or had temperature values much warmer than one could physically expect and were deleted with a threshold condition in the processing.

(b) Airborne radar data

The primary radar data set used in this study is the lower fuselage (LF) C-band radar data from the two NOAA* WP-3D aircraft (N42RF and N43RF, Table 1) obtained in 24 missions flown during the TOGA COARE (Fig. 3, Table 2). The LF radar reflectivity data are used to identify precipitating regions and classify the radar echo within those regions as corresponding to convective or stratiform precipitation using an objective algorithm (section 3(b)).

The LF radar scans 360° in the horizontal once a minute (Fig. 4). The elevation angle of the scan is tilted upward a few degrees to minimize intersection with the ocean surface. The small horizontal beam width (1.1°) permits detailed mapping of the horizontal pattern of reflectivity. In this study, data out to a range of 120 km from the aircraft were used, corresponding to a maximum horizontal beam width of 2.3 km. The vertical extent of the resolution volume over which the backscattered power is returned varies from a few hundred metres close to the aircraft to 8.6 km at 120 km range. Although the wide vertical beam width (4.1°) of the LF radar makes comparison of absolute reflectivities at different ranges problematic, only accurate relative reflectivities over local regions are necessary for application of the convective/stratiform separation algorithm. Additionally, the wide

* National Oceanic and Atmospheric Administration.

S. E. YUTER and R. A. HOUZE

TABLE 1.   SELECTED CHARACTERISTICS OF THE AIRBORNE RADARS USED IN THIS STUDY

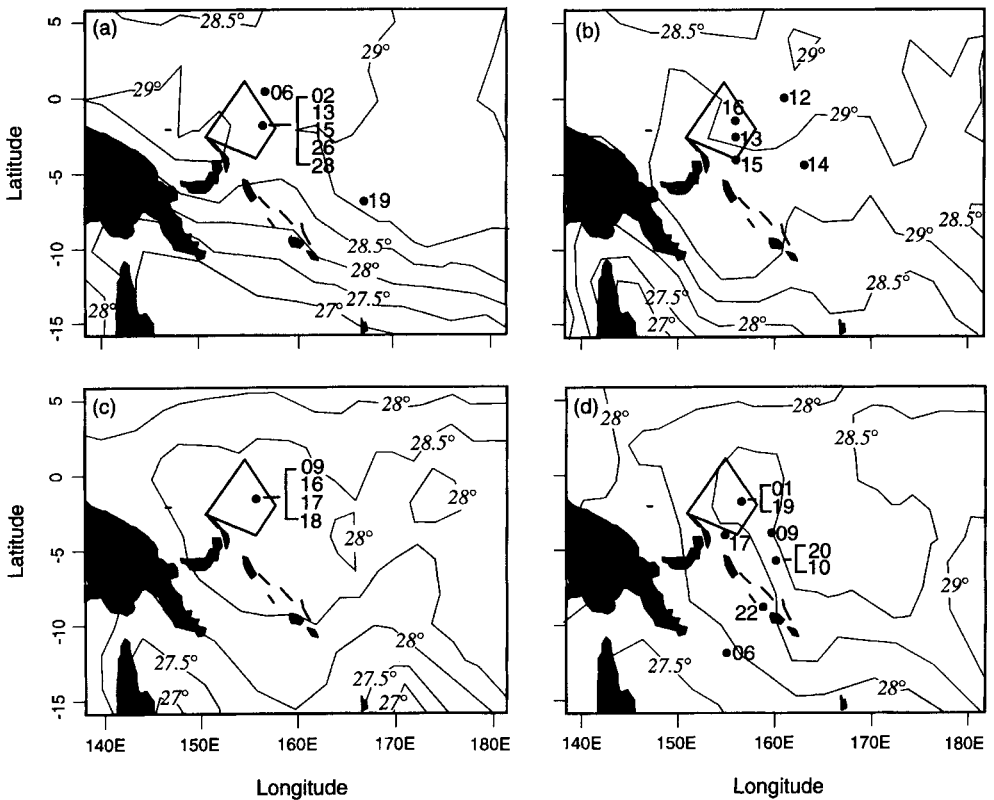|	NOAA WP-3D aircraft, N42RF and N43RF	
	Lower fuselage C-band	Tail X-band
Wavelength (cm)	5.59	3.22
Peak transmitted power (kW)	70	60
Beam width (degrees):		
horizontal	1.1	1.35
vertical	4.1	1.9
Pulse length (km)	0.9	0.075
Antennae rotation rate (degrees s^{-1})	6	60
Polarization	Horizontal	Vertical (N42RF) Horizontal (N43RF)

Figure 3.   Maps showing general location of WP-3D aircraft missions (the numbers refer to the day the mission occurred) during the TOGA COARE intensive observing period in relation to monthly sea surface temperature (SST, °C); (a) November 1992, (b) December 1992, (c) January 1993, and (d) February 1993. (Time-averaged NMC global SST analysis provided by Shuyi Chen.)

TABLE 2. DATA USED IN THIS STUDY FROM THE NOAA WP-3D AIRCRAFT MISSIONS

Date	Mission	Take-off/ landing times (UTC)	Location (lat, long E) (degrees)	Class	Synoptic-scale wind regime			Phase of the ISO
					Surface	850 hPa	200 hPa	
2 November 1992	H	2119/0551	−1.75, 156	1	SW	SW	E	A
6 November 1992	I	1406/2234	0, 157	3	SW	SW	E	A
13 November 1992	I	2104/0514	−1.75, 156	0	SE	SE	NE	S
15 November 1992	I	2157/0640	−1.75, 156	0	SW	N	NE	S
19 November 1992	I	1414/2032	−7, 167	2	SE	SE	NE	S
26 November 1992	I	2354/0824	−1.75, 156	1	W	SW	NE	S
28 November 1992	H	0206/0900	−1.75, 156	0	Calm	E	SE	S
12 December 1992	H	1402/2257	0, 160.5	3	NW	NW	NE	A
13 December 1992	I	1411/2238	−2.5, 156	4	NW	NW	E	A
14 December 1992	H	1301/2126	−4.5, 163	4	W	W	SW	A
15 December 1992	H	1513/2240	−4, 156	4	W	W	E	A
16 December 1992	H	2304/0831	−1.75, 156	1	SW	W	SE	A
9 January 1993	I	2056/0611	−1.75, 156	0	N	W	E	S
16 January 1993	H	2106/0442	−1.75, 156	0	NE	E	W	S
17 January 1993	I	2242/0754	−1.75, 156	1	E	E	W	U
18 January 1993	I	2242/0745	−1.75, 156	1 and 3	SE	SE	NW	U
1 February 1993	H	1918/0408	−1.75, 156	0	NW	NW	SE	U
6 February 1993	I	1418/2306	−12.5, 156.5	2	Cyclone	Rainband	W	A
9 February 1993	I	1420/2318	−4, 159.5	3	SW	W	E	U
10 February 1993	I	1802/0102	−6, 160	1 and 3	W	W	NE	A
17 February 1993	H	1809/0304	−4, 155	1	NW	NW	NE	A
19 February 1993	I	1905/0351	−1.75, 156	0	NW	NW	E	A
20 February 1993	I	1930/0412	−6, 160	2	W	W	SE	A
22 February 1993	I	1917/0243	−9, 159	4	W	W	E	A

Date designation is the UTC date on take-off. Mission: H indicates the N42RF aircraft, and I indicates the N43RF aircraft. Location is the approximate centre of the mission area. The cloud systems investigated by aircraft are categorized by mission class according to the largest cloud system's contiguous area of infrared cloud top colder than 208 K following Mapes and Houze (1992): Class 4—contiguous area of infrared cloud top colder than 208 K larger than 60 000 km², Class 3—between 20 000 and 60 000 km², Class 2—between 6000 and 20 000 km², Class 1—less than 6000 km², Class 0—no clouds with IR temperatures <208 K. Wind regime from the synoptic analysis of Bond and Alexander (1994). Active (A), suppressed (S) or unclassified (U) phase of the intraseasonal oscillation (ISO) from Chen et al. (1996) and Chen and Houze (1997).

vertical extent of the resolution volume is an asset in distinguishing between vertically oriented reflectivity maxima and thin layers of high reflectivity associated with a radar bright band.

When the aircraft was flying straight and level, five-minute composites of radar reflectivity centred on the mean position of the aircraft were created by interpolating* the radar data onto a 260 km × 260 km Cartesian grid with 2 km × 2 km resolution. During the five minutes, the aircraft travelled ∼35 km and the radar beam intersected any given 2 km × 2 km grid square several times. To minimize the effects of attenuation, the maximum reflectivity value intersecting each grid square was used. No filtering or smoothing was applied. The resulting radar-reflectivity map was input to the convective/stratiform separation algorithm (sections 3(b) and (c)). As part of the aircraft sampling plan, at 10–30 min intervals, the aircraft would execute a 2–4 min turn or quickly change altitude. LF composites could not be constructed during these time periods.

* The software to perform the interpolation of the aircraft data is called INTERPOL. The original version was written by Brian Mapes.
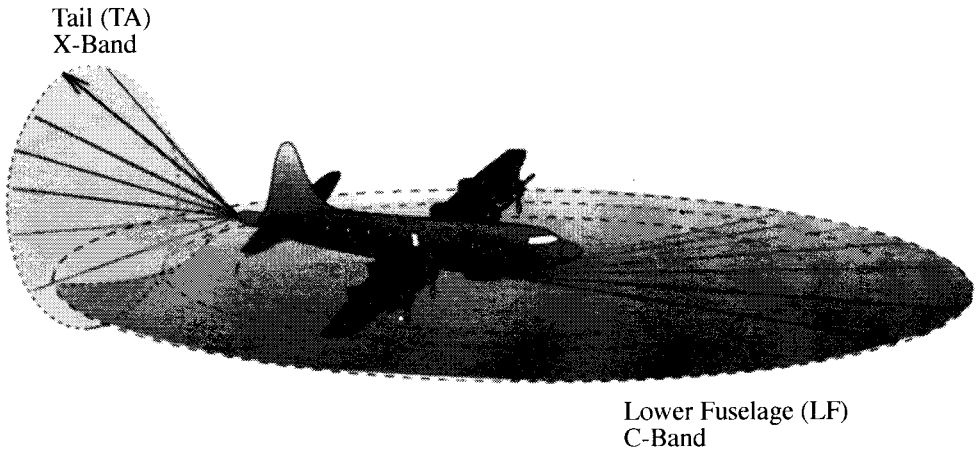
Figure 4.   Diagram of the scanning patterns of the lower fuselage (LF) and tail (TA) radars on the NOAA WP-3D aircraft. The TA radar scans both forward and aft at ±20° perpendicular to the aircraft track; only the aft scan is shown for clarity. The LF radar collects data out to 370 km range and the TA radar collects data out to 76.8 km range. See Table 1 for details on the characteristics of the radars.

In order to obtain nearly simultaneous measurements of spatially coincident radar echo and IR data, only LF composites obtained between 30 to 60 min after the hour were used. If the IR data were unavailable for that hour, the LF composites were deleted from the data set. Thus, the radar data are no more than ~20 min older or younger than the IR data. To obtain a reasonable sample size, 20 min is as close to simultaneous as could be achieved with these data sets. A total of 221 LF composites from 24 missions were used in this analysis.

Data from one LF radar were used per mission. If both NOAA WP-3D aircraft flew on a mission, data were used from the aircraft whose flight pattern sampled the larger area. For a given GMS IR image, several subsets of IR data corresponding to different LF composites obtained from the same aircraft during the 30 min period could be used. Using multiple LF composites within a 30 min period has the advantage of covering more area. Usually there was at least 5 min between the end of one composite and the start of the next. Depending on the flight-track pattern, these composites would have a spatial overlap of 60–100%. The LF composites within a given 30 min period are not independent. However, since individual convective cell lifetimes are ~30 min, there is not a unique relationship between precipitation structure and GMS satellite IR temperature over a given 30 min period. Data from overlapping composites result in a set of relationships between IR temperature and precipitation structure that span different stages of cell life cycles and thus are more representative of the range of conditions than any one arbitrary single LF composite–IR data pair. Using nearly simultaneous (<20 min difference) measurements from radar and satellite will increase the variance in the joint-probability distributions as compared with the hypothetical situation of using truly simultaneous measurements. Thus, the size of the regions within joint-probability space occupied by naturally precipitating cloud systems (section 7) will be overestimated.

Data from the tail radar on the NOAA WP-3D aircraft (Table 1) were used to tune the convective/stratiform separation algorithm for LF radar data and the TOGA COARE precipitation regime (sections 3(b) and (c)). The X-band tail radars map reflectivity and radial velocity at fine resolution in the vertical by scanning cones tilted approximately ±20° perpendicular to the aircraft heading (Fig. 4).

The LF radar data may include some non-meteorological echo that has to be removed from the data set. Ground clutter (radar return from islands) creates a strong echo that can be mistaken for convective activity (Figs. 5(a) and (b)). Sea clutter is caused by the reflection of the radar beam off the ocean surface. The pattern of the sea clutter is related to the altitude of the aircraft, the elevation angle of the radar beam, and the heights of waves on the ocean surface. At low altitudes (<100 m), the sea clutter is usually confined to a region within a few km of the aircraft track (Figs. 5(c) and (d)). At higher altitudes (~5 km) the sea clutter may occur in a circular pattern starting at a particular range from the aircraft and extending outward (Figs. 5(e) and (f)). The location of sea clutter moves with the position of the aircraft. National Center for Atmospheric Research (NCAR) Zebra software (Corbet *et al.* 1994) was used to view sequential LF composites to identify sea clutter, and to position the composites relative to a detailed island map to identify ground clutter.

(c) Active and suppressed conditions

To aid in relating our results to large-scale conditions, we note that large-scale convective activity in the western Pacific warm pool region is modulated over a 30–60 day period by the intraseasonal oscillation (ISO). The *active phases* of the ISO are marked by a large, generally eastward-propagating ensemble of cloud clusters containing embedded 2-day westward-propagating disturbances (Nakazawa 1995; Chen *et al.* 1996). In the *suppressed phases* of the ISO, these large cloud-cluster ensembles are mostly absent, although convective activity on smaller spatial and temporal scales still occurs. Three active ISO phases passed through the TOGA COARE region during the IOP (Chen *et al.* 1996). The data in the following discussion are categorized according to whether the corresponding aircraft mission investigated a region within an active or suppressed phase of the ISO based on the analysis of time–longitude plots of per cent high cloudiness by Chen *et al.* 1996 (Table 2). If the mission region did not clearly fall within an ISO phase, data from that mission are labelled as unclassifiable.

(d) Ancillary data

Several ancillary data sets are used to characterize the basic large-scale environmental conditions of the samples obtained within each aircraft mission (Table 2). The wind regime in the vicinity of each aircraft mission was obtained from the synoptic analysis of Bond and Alexander (1994). Additionally, Kingsmill and Houze's (1995) aircraft sounding data were used to describe some basic characteristics of storm-inflow air within two layers of the lower atmosphere from 500 to 1000 m and 5000 to 5500 m (Table 3).

(e) Fine and coarse resolution

The analysis of LF radar-reflectivity composites by the convective/stratiform (CS) separation algorithm produces a 240 km × 240 km CS map of 2 km × 2 km resolution pixels centred on the aircraft position. This map is divided into 100 *fine grid* squares of 24 km × 24 km each (Figs. 6(a) and 7(a)). Fine-resolution squares that contained any problematic data were deleted from the data set (Fig. 5). The area of convective precipitation and the area of stratiform precipitation were calculated for each remaining fine-grid element (Figs. 6(b) and (c), and 7(b) and (c)). The corresponding IR data for each fine-grid square in the CS map were averaged over a ~25 km × 25 km area to produce a mean IR temperature (Figs. 6(d) and 7(d)). Several factors prevented an exact fit of the IR data to the 24 km × 24 km CS map square. The IR data pixel boundaries rarely coincided with those of the radar grids. Since the IR data pixel size increases as a function of distance from the sub-satellite

TABLE 3. AVERAGE PRECIPITATION-REGION CHARACTERISTICS FOR SAMPLED REGIONS OF EACH AIRCRAFT MISSION AND BASIC MEASURED PARAMETERS FROM STORM-INFLOW SOUNDINGS

Mission date	Total precipitation area (% of coarse grid)	Convective area/total precipitation area (%)	Stratiform area/total precipitation area (%)	1 km wind direction (degrees)	1 km wind speed (m s⁻¹)	5 km wind direction (degrees)	5 km wind speed (m s⁻¹)	1 km temperature (°C)	5 km temperature (°C)	1 km water vapour (g kg⁻¹)	5 km water vapour (g kg⁻¹)
2 November 1992	6	18	82	217	4.82	251	2.58	23.43	−2.05	16.15	4.04
6 November 1992	41	4	96	249	7.63	174	6.83	22.19	−2.52	16.42	5.65
13 November 1992	3	32	68	126	4.22	082	4.57	22.83	0.06	15.86	2.33
15 November 1992	2	30	70	195	3.42	064	4.25	22.37	−2.69	15.42	3.67
19 November 1992	31	20	80	119	5.17	128	2.32	22.74	−2.08	16.07	3.18
26 November 1992	17	7	93	270	3.22	097	9.09	22.41	−2.12	15.15	3.47
28 November 1992	2	71	29	251	1.62	078	3.89	22.68	−1	16.06	3
12 December 1992	52	2	98	NA	NA	NA	NA	NA	NA	NA	NA
13 December 1992	52	3	97	NA	NA	NA	NA	NA	NA	NA	NA
14 December 1992	52	7	93	275	8.25	169	2.25	21.99	−2.13	16.49	4.31
15 December 1992	76	9	91	215	8.43	173	5.29	22.77	−0.77	16.16	4.44
16 December 1992	11	16	84	246	5.09	028	4.46	22.83	−0.93	15.59	4.55
9 January 1993	4	24	76	045	3.02	305	3.2	22.58	−1.23	16.56	3.58
16 January 1993	20	9	91	092	6.82	278	1.63	22.7	−0.9	15.95	2.95
17 January 1993	11	10	90	NA	NA	NA	NA	NA	NA	NA	NA
18 January 1993	43	3	97	111	8.44	268	1.96	22.58	−0.97	16.15	5.59
1 February 1993	1	16	84	300	10.04	276	9.28	22.75	−3.67	15.04	4.86
6 February 1993	31	6	94	044.5	5.5	296	14.32	22.25	−1.83	15.54	5.9
9 February 1993	42	2	98	NA	NA	NA	NA	NA	NA	NA	NA
10 February 1993	24	1	99	247	10.01	229	4.77	23.02	−2.12	15.62	4.56
17 February 1993	14	16	84	NA	NA	NA	NA	NA	NA	NA	NA
19 February 1993	0.1	7	93	300	9.9	281	4.13	23	−1.87	13.87	5.46
20 February 1993	41	6	94	NA	NA	NA	NA	NA	NA	NA	NA
22 February 1993	58	5	95	290	11.84	293	7.27	22.71	−1.52	15.18	6.05

NA = not available.
The storm-inflow soundings were provided by David Kingsmill. Inflow sounding characteristics are layer averages from 500 to 1000 m and 5000 to 5500 m.
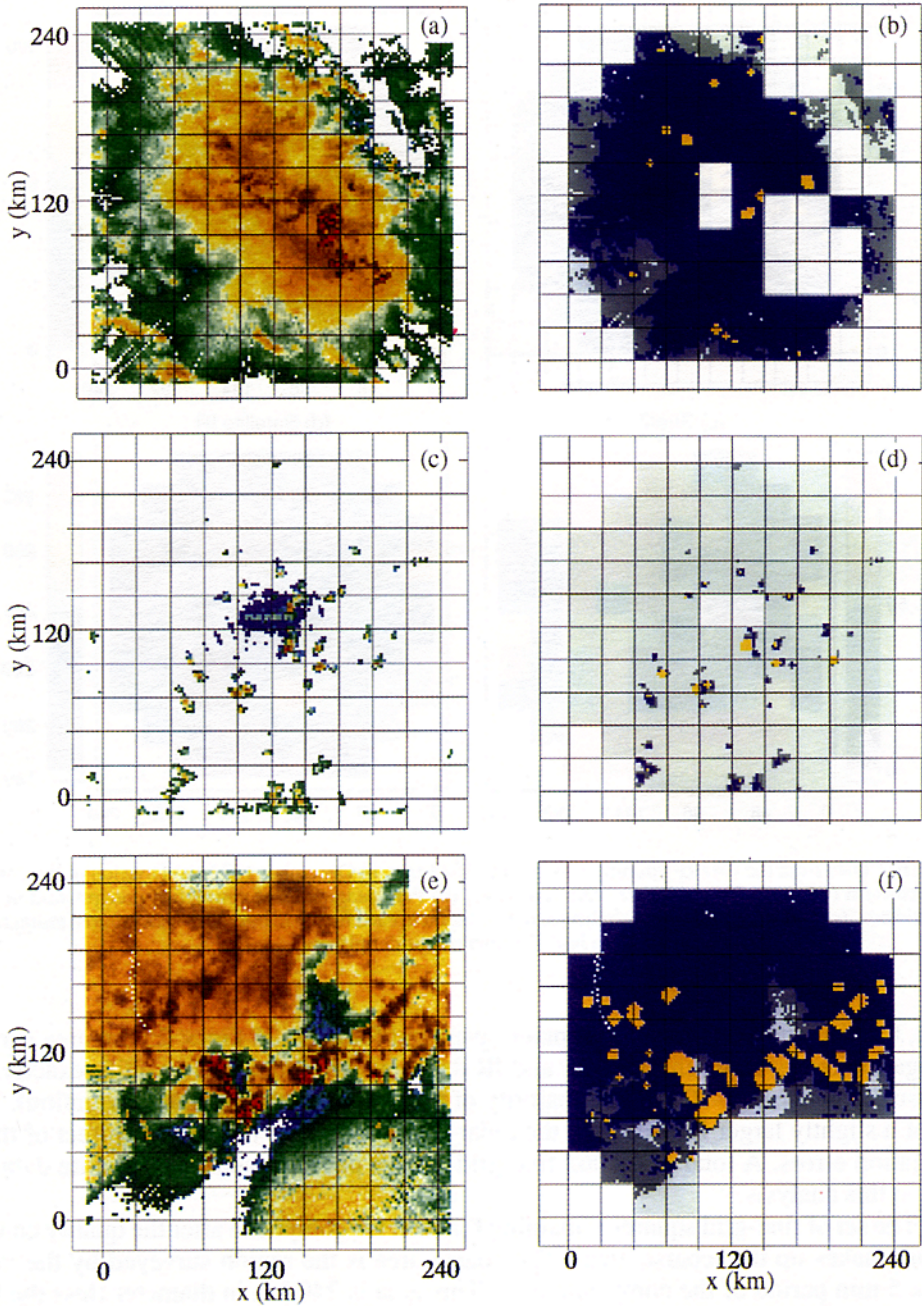
Figure 5. Examples of non-meteorological echo in the lower fuselage radar-reflectivity composites (left column) and edited coarse area convective/stratiform (CS) maps (right column) with fine-grid squares overlaid. Quality-control editing removes entire fine-grid squares from the CS maps. (a) and (b) 0045 UTC 22 February 1993 containing ground clutter from islands, (c) and (d) 0048 UTC 10 January 1993 containing sea clutter when aircraft is at low altitudes, (e) and (f) 1940 UTC 15 December 1992 containing sea clutter when aircraft is at ~5 km altitude. Reflectivity values increase as colours change from blues to greens to oranges to reds. White areas indicate no echo. The CS map colours correspond to the following: yellow: convective, blue: stratiform, dark grey: weak echo, and light grey: no echo.
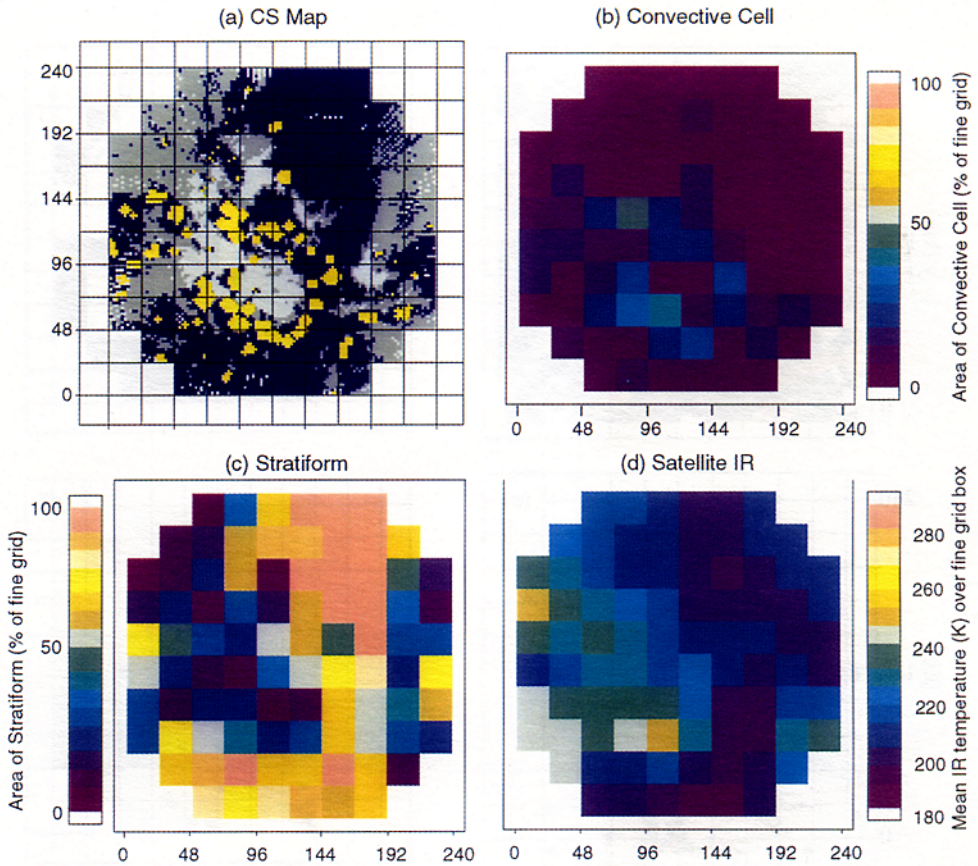
Figure 6.   Data from the N42RF aircraft from 1940 to 1945 UTC 14 December 1992. (a) Division of the convec-
tive/stratiform (CS) map for coarse area into fine grids. (b) Percentage area of convective precipitation in each
fine-grid box. (c) Percentage of area of stratiform precipitation in each fine-grid box. (d) Mean infrared temperature
in each fine-grid box. CS map colour definitions as in Fig. 5.

point, the size and exact number of pixels averaged for the ~25 km × 25 km area varied.
Navigation errors between the radar and IR data sets are difficult to quantify exactly but
are usually between 5–10 km (the majority of the error is in the satellite navigation). The
use of a slightly larger IR area than the radar fine-grid square reduces the effect of these
navigation errors. A total of 18 062 fine-grid-square pairs of radar and satellite data are
used in this analysis.

   The set of fine-grid squares remaining for each LF composite after the quality control
editing makes up the 'coarse area'. The coarse area is the region surveyed by the radar
in the 5 min period of the composite map. This area is 240 km in diameter (less the fine
grids removed because of clutter echo). Since a 240 km diameter area is of the order of
the resolution of a GCM we call it a coarse area to distinguish it from the 24 km scale
fine grids, which are similar to the grid resolution of a mesoscale model. By analysing
the satellite and radar data on both fine and coarse resolutions, we attempt to relate our
empirical results to both small- and large-scale model frameworks.

   Over 75% of the 221 coarse areas in the data set have an area greater than 90% of
the potential maximum area of 50 688 km^2 (no non-meteorological echo is present and
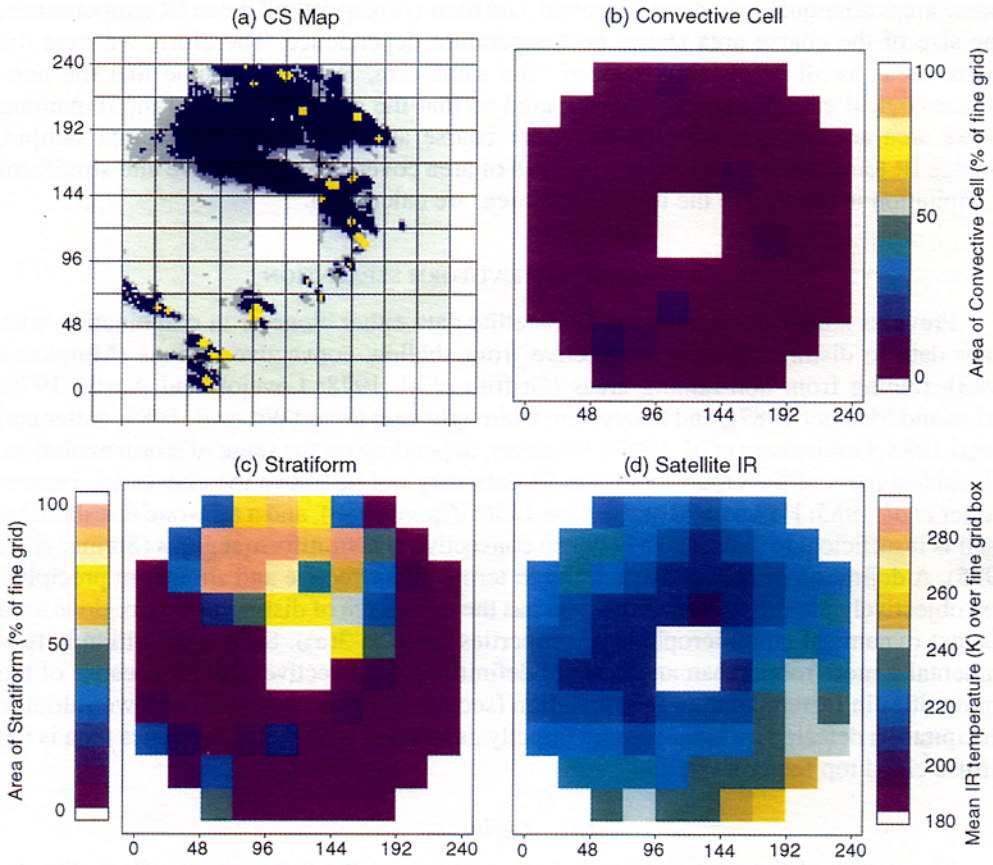only the 12 corner fine-grid squares are removed). Figure 8 shows the range of sizes of the

Figure 7.   As Fig. 6 but for the N43RF aircraft. Data from 0241 to 0246 UTC 28 November 1992.
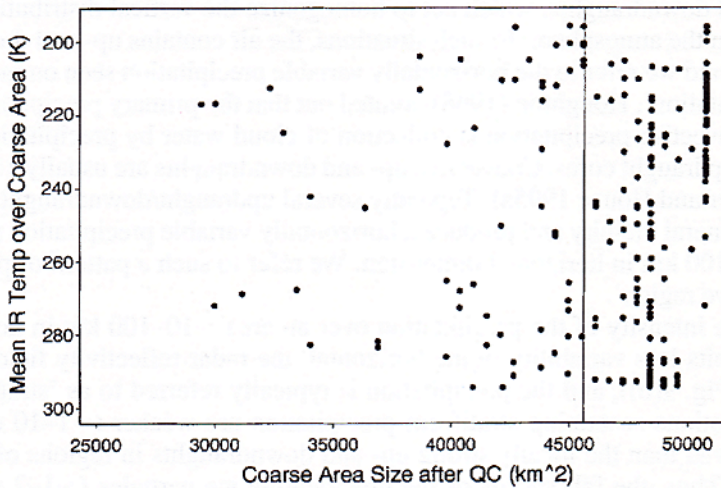

Figure 8.   Scatter plot of the size of each coarse-area sample after quality control (QC) versus average infrared (IR) temperature over the coarse area. The vertical line is at 90% of the maximum possible area.

coarse areas after quality control is applied, and their corresponding mean IR temperatures. The size of the coarse area shows no temperature dependence. Therefore, we treat the coarse areas as all being approximately the same size. We thus assume that the non-meteorological echo is randomly distributed so that the characteristics of the remaining coarse area are representative of the entire coarse area. For each coarse-area sample, average IR temperature, and the percentages of area covered by convective and stratiform precipitation in relation to the total coarse area, are calculated.

3. CONVECTIVE/STRATIFORM SEPARATION

Previous studies have analysed IR satellite data either alone or in combination with radar data to distinguish deep convective from shallow convective regions (Murakami 1983), raining from non-raining areas (Griffith *et al.* 1978; Lovejoy and Austin 1979; Arkin and Meisner 1987), and heavy-rain from light-rain areas (Wu *et al.* 1985; Adler and Negri 1988; Goldenberg *et al.* 1990). However, depending on the stage of storm evolution, the coldest parts of the cloud top in the IR data may not lie above the convective centres (Adler *et al.* 1983; Heymsfield and Fulton 1988; Zipser 1988), and a rain-rate threshold by itself is insufficient to distinguish between convective and stratiform regions (Steiner *et al.* 1995). A definition of convective activity in terms of convective and stratiform precipitation objectively identified from radar data has the advantage of distinguishing regions with distinct dynamical and microphysical properties (section 3(a)). Such a definition is fundamentally more robust than an IR-based definition of convective activity because of the ambiguities in IR temperature interpretation (section 2(a)) and because the lower-altitude precipitation detected by radar is more directly associated with storm dynamics than is the diffuse cloud top seen by satellite.

(a) Definition

The nature of the precipitation field in a region of the atmosphere reflects the nature of the vertical air motions in that region. When the intensity of the precipitation exhibits strong variability in the horizontal, and radar echoes consist of vertical columns of high reflectivity (Fig. 9(a)), the air is usually in a state of convection characterized by strong up- and downdraughts, which act to homogenize the vertical distribution of moist static energy in the atmosphere. In such situations, the air contains up- and downdraughts $\sim$1–10 m s^{-1} and we refer to the horizontally variable precipitation seen on radar as 'convective precipitation'. Houghton (1968) pointed out that the primary precipitation-growth process in convective precipitation is collection of cloud water by precipitation particles in the strong updraught cores. Convective up- and downdraughts are usually 1–6 km in dimension (Yuter and Houze 1995a). Typically several updraught/downdraught pairs occur in the same general vicinity and produce a horizontally variable precipitation pattern over an area $\sim$10–100 km in horizontal dimension. We refer to such a pattern of precipitation as a 'convective region'.

When the intensity of the precipitation over an area $\sim$10–100 km in horizontal dimension exhibits less variability in the horizontal, the radar-reflectivity field appears to be in layers (Fig. 9(b)), and the precipitation is typically referred to as 'stratiform'. The upward air motions sustaining stratiform precipitation are weaker ($\sim$1–10 cm s^{-1}) but more widespread than the locally strong up- and downdraughts in regions of convective precipitation. Thus, the fall speeds of the precipitating ice particles ($\sim$1–2 m s^{-1}) (Locatelli and Hobbs 1974) far exceed the magnitude of the vertical air motion. Houghton (1968) pointed out that under these conditions the primary precipitation-growth process is vapour deposition on ice particles, a slow process, and particles must fall from near cloud
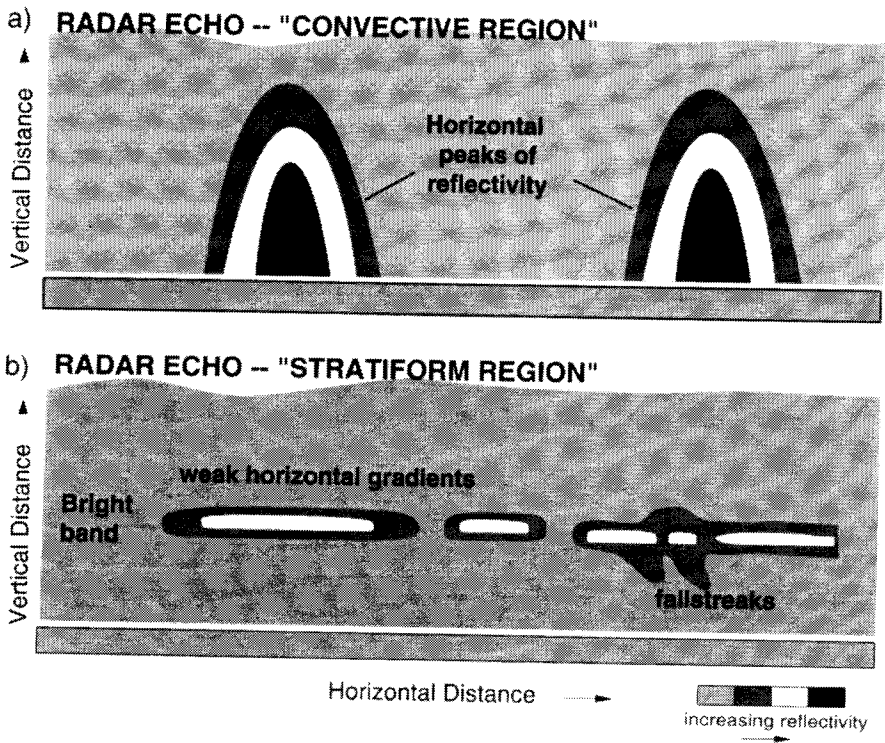
Figure 9. Characteristics of (a) convective and (b) stratiform precipitation regions on radar. Convective regions are 10–100 km in horizontal dimension and contain vertically oriented local maximum in reflectivity associated with the locations of updraughts with vertical air motions of sufficient magnitude to favour growth of precipitation particles by collection (coalescence and/or riming). These local maxima correspond to peaks in the horizontal reflectivity field. The reflectivity field for the stratiform precipitation region has a layered appearance, often with a layer of maximum reflectivity occurring just below the 0 °C level (radar bright band). Air motions in stratiform regions are of insufficient magnitude to keep precipitation particles suspended aloft and thus the primary precipitation-particle growth is by condensation and vapour deposition of slowly falling particles. In the horizontal, at a given level, the reflectivity field of stratiform precipitation regions is relatively homogeneous and does not contain intense localized maxima. Fall streaks may emanate from the bright-band layer but generally do not reach the surface.

top to attain the maximum possible growth by vapour diffusion. Stratiform precipitation areas are thus distinct from convective areas by virtue of particles always settling downward and growing slowly by deposition of vapour, in contrast to the convective updraught cores, where large concentrations of droplets condense rapidly and are readily available for collection by larger precipitation particles.

When a convective updraught weakens, many ice particles grown by the collection of cloud droplets and carried up to the top of the cell during the active phase of the convective updraught slowly fall out through the weaker upward motion while continuing to grow by vapour diffusion. The once-convective precipitation core thus turns into a region of stratiform precipitation. Weakening of convective cells appears to account for a large portion of the stratiform-appearing radar echo over the tropical ocean. In this sense, the designation stratiform does not imply that the precipitation was not convective in origin, but rather that the dominant air motions and precipitation-growth processes have changed over from the collection-dominated vertical columns of strong radar echo to the vapour-diffusion-dominated broad layers characterized by downward drifting ice particles formed earlier in updraughts but stranded aloft as the upper regions of convective updraughts

weaken. As the parcels of air in the convective updraughts rising out of the boundary layer reach the upper atmosphere, they broaden and flatten as a result of the decreasing pressure and because they have reached their level of neutral buoyancy (Lilly 1988; Yuter *et al.* 1995). As more and more weaken, spreading convective elements arrive in the upper troposphere, they congregate there and eventually amalgamate to form a large horizontal area, which we identify as the 'stratiform region' on radar.

Within convective and stratiform precipitation regions, the joint variation of precipitation processes and vertical mass transport of air within a column of an instantaneous storm volume create different characteristic vertical profiles of radar reflectivity, divergence, latent heating, and momentum transport (Houze 1989; Mapes and Houze 1995; Yuter and Houze 1995a,b; Yang and Houze 1996). Thus, the subdivision of precipitation into convective and stratiform regions as defined above aids in understanding the storm as a whole in terms of the contributions of these physically distinct components.

(b) Algorithm description

The convective/stratiform separation algorithm uses radar-reflectivity data interpolated to 2 km × 2 km spatial resolution. The vertically oriented regions of higher relative echo intensity characteristic of convective cells (Fig. 9(a)) are manifested as regions of local two-dimensional peakedness in the horizontal reflectivity field. These regions of local two-dimensional peakedness are classified as convective, and the remaining reflectivity echo is classified as stratiform (Churchill and Houze 1984; Steiner *et al.* 1995). The method has been verified as consistent with the vertical air motions associated with convective versus stratiform regions (section 3(a)) using high-resolution dual-Doppler vertical-velocity data from ground-based radars (Steiner *et al.* 1995).

Convective cell region centres are identified when the difference (ΔZ_{bg}) between the reflectivity of an individual grid point and the local background reflectivity (the average of the radar-reflectivity factor of non-zero radar echoes within a radius of 11 km around the grid point) exceeds a convective-centre criterion (ΔZ_{cc}) (Churchill and Houze 1984; Steiner *et al.* 1995). Once the convective centres have been identified, grid points within a certain radius of the convective centre are classified as convective. We used the radii from Steiner *et al.* (1995), which are a function of background reflectivity. Thus, pixels within these radii of the convective core, although they do not themselves meet the peakedness criteria, are also classified as convective. We had to modify the Steiner *et al.* (1995) convective-centre criterion slightly to work with NOAA WP-3D LF radar-reflectivity data interpolated to 2 km × 2 km resolution. The convective-centre criterion was changed to a cosine function of the form:

$$\Delta Z_{cc} = a \cos \left(\frac{\pi Z_{bg}}{2b} \right). \tag{1}$$

This function has the same basic shape as the function used by Steiner *et al.* (1995). However, Eq. (1) is continuous and easily adjusted by setting the parameters a and b. Adjustments to a and b are necessary to tune the algorithm to work properly with data from a particular radar and climatic regime (seasonal and/or geographic). The algorithm was tuned by setting a and b such that the resulting objective classifications of the LF reflectivity map into convective and stratiform were most consistent with a subjective classification of precipitation type based on high-resolution vertical cross-sections of reflectivity and radial velocity from the NOAA WP-3D tail radar. The idea of the tuning is to use the bright band and other evidence of uniformity in the horizontal, such as laminar flow, as 'truth' of the presence of stratiform precipitation. If the algorithm calls any precipitation of this type

convective, it is deemed to be in error. The values of a and b that minimize this error are sought. This method of tuning the algorithm to agree with the implied vertical-velocity structure of the radar-echo pattern is exactly the same procedure as followed by Steiner *et al.* (1995). Tuning could be done only at ranges <40 km from the aircraft since the X-band radiation of the tail radar rapidly attenuates. At farther ranges, the conditions that can lead to misclassifications are lessened by the widening vertical beam width. Best results for the TOGA COARE LF data were found when $a = 8$ and $b = 64$.

When the aircraft was above 1 km altitude, the 4° vertical beam width of the LF radar would often intersect with the radar bright band and result in smooth regions of high reflectivity at close ranges to the aircraft in the LF composite. At aircraft altitudes less than 1 km, intersection of the beam with the bright band at close ranges was geometrically infeasible. At these low altitudes an additional criterion of an intensity threshold (Steiner *et al.* 1995) was applied to identify convective centres such that if the reflectivity of the pixel was $\geqslant 46$ dBZ it was also labelled as a convective centre. A weak-echo category <15 dBZ (<0.5 mm h^{-1} rain rate) was introduced since some types of sea clutter (non-meteorological echo caused by the intersection of the radar beam with the ocean surface, section 2(e)) and weak precipitation echo are difficult to distinguish on the LF maps.

(c)   Application of convective/stratiform algorithm

The convective/stratiform separation algorithm can be applied within ranges from the radar where the Cartesian grid resolution of 2 km is larger or approximately equal to the radar horizontal beam width. The implementation of the separation algorithm for this study analyses* the input LF reflectivity composites into 240 km × 240 km CS maps. Each 2 km × 2 km grid element is assigned one of four categories: convective, stratiform (not convective and >15 dBZ), weak echo (⩽15 dBZ) and no echo. Grid elements at the corners, whose range from the centre was greater than 120 km (2.3 km horizontal beam width), were deleted since performance of the convective/stratiform algorithm was unreliable at beam widths greater than 2.3 km.

Although determining the algorithm parameters a and b was based on subjective judgment of vertical cross-sections, the tuned performance of the algorithm was considered acceptable since it worked reasonably well over a wide variety of conditions observed during the TOGA COARE. The algorithm is general enough to include rain showers from warm clouds (when they are big enough to be seen by radar). If the warm-rain echoes are strong enough, the algorithm identifies them as convective; the weaker rain echoes associated with weak updraughts incapable of supporting precipitation particles are identified as stratiform. The algorithm has difficulty distinguishing between embedded convection and heavy fall streaks (Houze 1993, pp. 205–208) within stratiform regions. These transitional regions were sometimes classified as convective and sometimes as stratiform. The transitional regions are often difficult for objective algorithms to distinguish, and indeed it is often unclear from a subjective evaluation of the data whether they should fall within the convective or stratiform classes. We tuned the algorithm such that transitional regions would tend to be labelled as stratiform rather than convective. This decision is based on the results of Yuter and Houze (1995a), in which statistical analysis of simultaneous high-resolution measurements of radar reflectivity and dual-Doppler vertical velocity showed that the most commonly occurring vertical air motions within transitional regions were weak and stratiform in character before the reflectivity pattern appears fully uniform in vertical cross-sections.

---

* The convective cell/stratiform separation region requires a border area of data in order to analyse out to the edge of its effective range correctly.
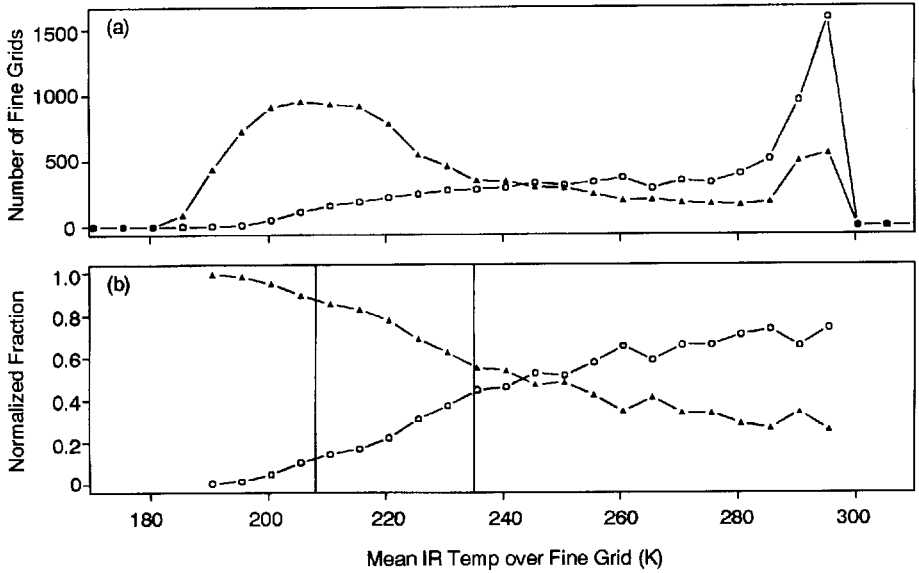
S. E. YUTER and R. A. HOUZE

Figure 10. (a) Frequency distribution of infrared (IR) temperature of fine grids containing any amount of precipitation (triangles) and no precipitation (circles). Histogram bin width is 5 K. (b) Mean IR temperature over the fine grid versus normalized fraction of fine grids containing any amount of precipitation (triangles) and no precipitation (circles). Horizontal lines indicate 208 and 238 K.

Comparison of different objective convective/stratiform separation algorithms has shown that convective and stratiform *area* statistics are not particularly sensitive to the specific separation algorithm used as long as the algorithm is reasonable (Steiner *et al.* 1995; NASA Tropical Rainfall Measuring Mission Ground Validation Algorithm Intercomparison Workshop, Dec. 1994). It is only when rain fractions are computed by applying convective and stratiform rain rates or reflectivity to rain-rate relations to these areas that the differences between separation algorithms may produce qualitatively different results. To mitigate the impact of uncertainties inherent in the calculation of rain fractions, this study will primarily focus on characteristics of the precipitation regions that are relatively insensitive to the particular algorithm employed and thus are more robust: the areas of the precipitation regions, convective regions and stratiform regions respectively.

4. PRECIPITATION STRUCTURE AND IR TEMPERATURE AT FINE RESOLUTION

For each of the 18 062 fine-grid squares, we compared mean IR temperatures with occurrence of precipitation, areal coverage by precipitation, and existence and areal coverage of stratiform and convective precipitation.

(a) Probability of occurrence of precipitation

A basic characteristic of clouds is whether or not they are precipitating. Precipitating regions are defined as containing convective and/or stratiform precipitation in the CS maps. Figure 10(a) shows the mean IR temperature of fine-resolution elements sampled by aircraft radar with and without precipitation. These data sum to the histogram of IR sampling by aircraft in Fig. 2(c). The number of counts in the frequency distribution is normalized by the total number of points in each 5 K IR temperature bin to produce Fig. 10(b), the probability that a 24 km × 24 km fine grid contains precipitation as a
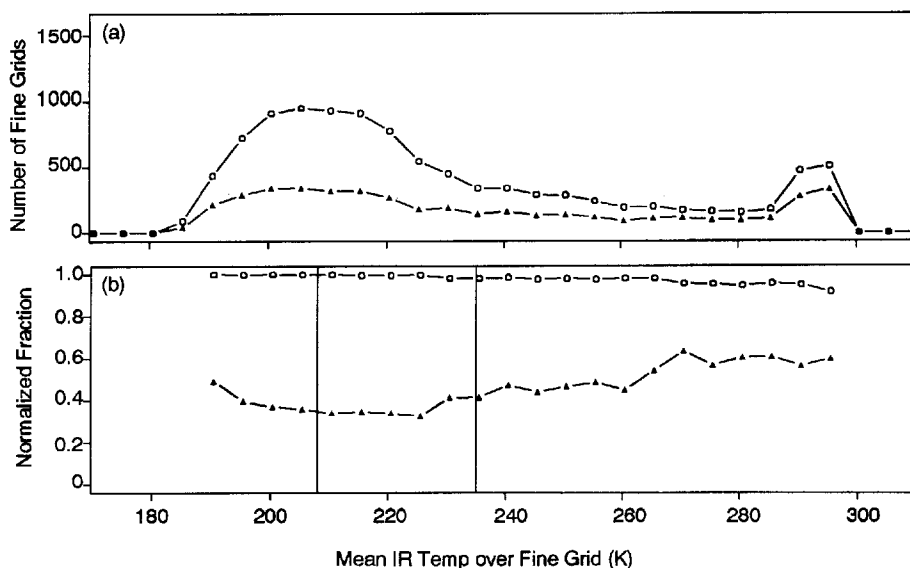
Figure 11. (a) Frequency distribution of infrared (IR) temperature within precipitating fine grids containing any amount of convective (triangles) and stratiform (circles) precipitation. Histogram bin width is 5 K. (b) Mean IR temperature over the fine grid versus normalized fraction of precipitating fine grids containing any amount of convective precipitation (triangles) and stratiform precipitation (circles). Horizontal lines indicate 208 and 238 K.

function of average IR temperature. As the IR temperature increases, the probability of a fine grid containing any precipitation decreases. At 245 K the odds are even that the fine-resolution grid element contains precipitation.

Various temperatures between 235 and 208 K have been used as indicators of precipitation in instantaneous IR data (see discussion by Mapes and Houze (1993)). Within the western Pacific convective activity analysed in this study, there is a 55% probability that some precipitation occurs in fine-grid elements whose mean IR temperature is 235 K. At a mean IR temperature of 208 K over a fine-grid element there is an 88% probability of some precipitation within that grid square. Although warm clouds cannot be unambiguously identified with IR data alone because of the beam-filling problem, previous studies have established that the probability of precipitation from maritime warm clouds (tops entirely below the 0 °C level) increases with increasing cloud-top height (Byers and Hall 1955).

(b) Occurrence of stratiform and convective precipitation

The distribution of the occurrence of convective and stratiform precipitation within fine-grid squares that contain precipitation is shown in Fig. 11(a). Since an individual grid square may contain both convective and stratiform precipitation, these histograms do not sum to the histogram of IR temperature of precipitating fine-grid elements in Fig. 10(a). Both convective and stratiform precipitation occurred at all IR temperatures between 188–298 K. The probability of a precipitating fine-grid square of a given mean IR temperature containing any amount of stratiform or convective precipitation is illustrated by the normalized IR temperature distribution in Fig. 11(b). Normalization is accomplished by dividing the convective and stratiform histograms in Fig. 11(a) by the total number of grid squares containing precipitation (Fig. 10(a)). All precipitating fine-resolution squares have a greater than 90% probability of containing at least some stratiform precipitation,
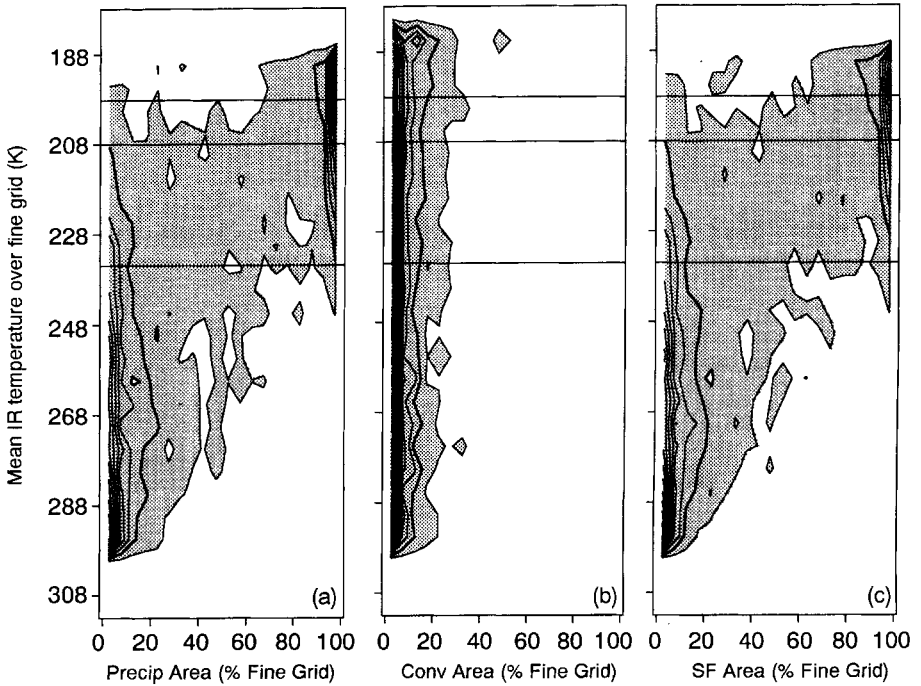
Figure 12.   Contoured joint-probability diagrams of percentage area of precipitating fine grids containing (a) total precipitation, (b) convective precipitation, and (c) stratiform precipitation. The histogram bin sizes are 28.8 km² (5% of fine grid area) and 5 K. Plot is contoured at intervals of 0.2% data per K per km², starting at 0.1% K⁻¹km⁻² with the 0.3% K⁻¹km⁻² contour highlighted. Horizontal lines indicate 200, 208 and 235 K.

independent of IR mean temperature. The probability of stratiform precipitation within a precipitating fine-resolution square is virtually 100% at mean IR temperatures <225 K. In contrast, the likelihood that a precipitating fine-grid element contains convective precipitation generally *decreases* from 60% to 35% with decreasing mean IR temperature from 298 to 208 K. At temperatures <208 K, the probability of a precipitating fine-grid element containing convective precipitation increases up to ~50%.

(c)   Areal coverage by stratiform and convective precipitation

The relationships between the area of convective and stratiform precipitation as a function of mean IR temperature are shown in contoured joint-probability diagrams in Fig. 12. The contours show the relative frequency of occurrence of different sizes of precipitation areas at a given mean IR temperature at fine resolution. These diagrams resemble the contoured frequency by altitude diagrams (CFADs) of Yuter and Houze (1995a) except that, in this case, the mean IR temperature of the fine-grid element serves as the altitude coordinate. The distribution of precipitation-area size is strongly skewed to small sizes, less than 10% of a 24 km × 24 km fine-grid element, for fine-grid elements with mean IR temperature higher than 235 K (Fig. 12(a)). At lower temperatures the distribution of precipitation area is much broader, and the majority of points occur at near 100% coverage of the fine-grid area. The full size range of precipitation regions is not encompassed by 0–100% coverage of the fine-grid area of 576 km². Thus, the statistics of the fine-grid areas can contain a 'pile up' of grid elements with 100% coverage, representing parts of regions greater than 576 km² in size. The local maximum at 100% at lower

temperatures in Figs. 12(a) and (c) are indicative of regions larger than the fine-grid area. For fine-resolution elements containing precipitation, *the area of precipitation generally increases with decreasing mean IR temperature* (Fig. 12(a)). Coverage by precipitation is most commonly less than 30% of the fine-grid area at mean IR temperatures >250 K. Completely filled grid squares rarely occur at temperatures >245 K. At 225 K, fine-grid elements 100% filled with precipitation occur more frequently than lesser coverages. As the IR temperature decreases below 225 K the frequency of 100% coverage increases slightly. In contrast, Fig. 12(b) shows that the area covered by convective precipitation in a fine-resolution square is nearly always less than 20% (<116 km^2); greater than 20% areal coverage is extremely infrequent. At mean IR temperatures <190 K there is a very slight increase in frequency of coverage by convective precipitation. *Thus, the area of the convective region is generally <20% of the 24 km $\times$ 24 km grid element and is essentially independent of mean IR temperature over the 24 km $\times$ 24 km fine-grid element.* This result implies that *an IR temperature threshold is not an effective method of distinguishing convective regions embedded within cloud clusters.* Deep clouds contain *both* convective and stratiform precipitation. Methods that use high cloudiness as a proxy for convective precipitation area will grossly overestimate the size of the underlying convective region. Since the area of contiguous convective precipitation is usually limited to a scale smaller than the fine-resolution element, we conclude that the convective activity is dispersed. The frequency distribution of stratiform precipitation (Fig. 12(c)) is similar to that of precipitation as a whole (Fig. 12(a)) and exhibits a trend of increasing coverage of stratiform precipitation with decreasing temperature. These results suggest that mesoscale models with grid elements $\sim$20 km in dimension are justified in parametrizing convective, but not the stratiform, precipitation which often fills the fine-grid element. At grid resolutions finer than 20 km the scale separations on which convective parametrizations are often based (Emanuel 1994, chapter 16) are likely invalid.

(d)   Significance of the life cycle of convective cells

Very cold fine-grid elements (<200 K) have a 50% probability of containing convective precipitation, and the area of that convective precipitation is most frequently less than 20% of the fine-grid area. In comparison, there is a nearly 100% probability that the very low IR temperature regions contain stratiform precipitation, usually over greater than 90% of the fine-grid element. Thus, instantaneously, *the coldest cloud tops are more commonly associated with stratiform precipitation.* These statistics confirm Zipser's (1988) and Heymsfield and Fulton's (1988) case-study observations showing that the low IR brightness temperatures do not generally overlie the convective region.

Most of the aircraft radar sampling occurred well after convection initiation, which will have some effect on the results. Maddox *et al.* (1986) and Zipser (1988) have observed that the relationship between cold cloud-top temperatures and precipitation structure varies during the life cycle of the storm. The coldest cloud tops are progressively displaced from the areas of convective activity as the storm evolves. Additionally, the area of cold cloud tops expands rapidly in the early stages of storm evolution and continues to expand for several hours *after* the area of intense radar echoes associated with convective precipitation begins to decrease (Zipser 1988).

During the initial stages of storm evolution, the coldest cloud tops present, almost by definition, would have to be in the close vicinity of convective cells. During the early stages of the storm, both high resolution (80 m) and coarse resolution (8 km) IR data can identify distinct cold regions associated with overshooting cumuliform features (Adler *et al.* 1983). However, this stage does not last very long (usually about 30 min or less) (Adler *et al.* 1983). The contiguous regions of cold cloudiness associated with cloud clusters larger

than 100 km in dimension last from 2–20 hours (Chen and Houze 1997). Therefore, it is more likely that a random snapshot will capture a stage of storm evolution when the coldest region does not overlie the convection.

There are competing hypotheses to explain the observation that the coldest cloud tops do not overlie the convective region after the initial stages of storm evolution. Some have argued that the displacement of cold cloud tops from the convective region is a result of the front-to-rear advection of air parcels that originate in the convective cells and overshoot their level of neutral buoyancy (Heymsfield and Fulton 1988). An alternate hypothesis accounts for the cold cloud temperatures kinematically by the adiabatic cooling of gently ascending and horizontally expanding air at the top of the stratiform region (Fritsch and Brown 1982; Zipser 1988). This second explanation is more consistent with the observation that the supply of overshooting air parcels is extremely limited since the vast majority of air parcels from the convective cells are slowed and stopped during their ascent and do not reach cloud top (Raymond and Blyth 1986, 1989; Yuter and Houze 1995b). In a recent numerical study, Pandya and Durran (1996) give strong support to the second hypothesis. They give a dynamical basis to the arguments of Fritsch, Brown and Zipser by showing that mesoscale lifting and cooling in the stratiform region are part of the nonlinear full-spectrum gravity-wave response to the distribution of heating in a region of convection. Additionally, they show that overshooting tops are *not required* to produce upper-level cooling in the stratiform region. Given the results of these studies, the very low IR temperatures in the stratiform regions seem most likely a result of adiabatic ascent.

5.   PRECIPITATION STRUCTURE AND IR TEMPERATURE AT COARSE RESOLUTION

At coarse resolution the area of the contiguous precipitation areas sampled by aircraft radar was usually* either of a comparable size or smaller than a coarse area. Hence, the statistics on the coarse scale are characteristic of the precipitating regions as a whole, and we obtain a broader range of results than was possible for the fine-resolution analysis.

(a)   Cloudy area and precipitation area

The area fractions of cloudy versus non-cloudy air are important terms in the large-scale heat and radiation budgets of the storm (Houze 1982). A very conservative measure of clear-air fraction is the area of pixels within a coarse area with IR temperatures less than 293 K. It is impossible with these data to tell for certain whether GMS IR high-resolution pixels with these IR temperatures truly contain no clouds, but it is a reasonable approximation. Using this definition of clear-air fraction, Fig. 13 shows that the coarse area was completely filled by clouds when precipitation areas were larger than ~25% of a coarse area. When precipitation areas were extremely small (<10% of a coarse area) the clear-air fraction had tremendous variability. These results imply that *clouds producing precipitation regions larger than 20% of a coarse area rapidly spread ice over a wide area beyond the boundaries of the precipitating clouds.*

(b)   Characterization of IR temperature over a coarse area

(i)   *Frequency distribution of IR temperature in the coarse areas sampled by aircraft radar.*   A variety of measures have been used to characterize the frequency distribution of IR temperatures at coarse scales (e.g. Arkin 1979; Murakami 1983). To examine the

---

* Notable exceptions occurred on 13 and 24 December 1992, the latter observed by shipborne radar, when the precipitation areas were of enormous size (see Fig. 12 of Chen *et al.* (1996)).
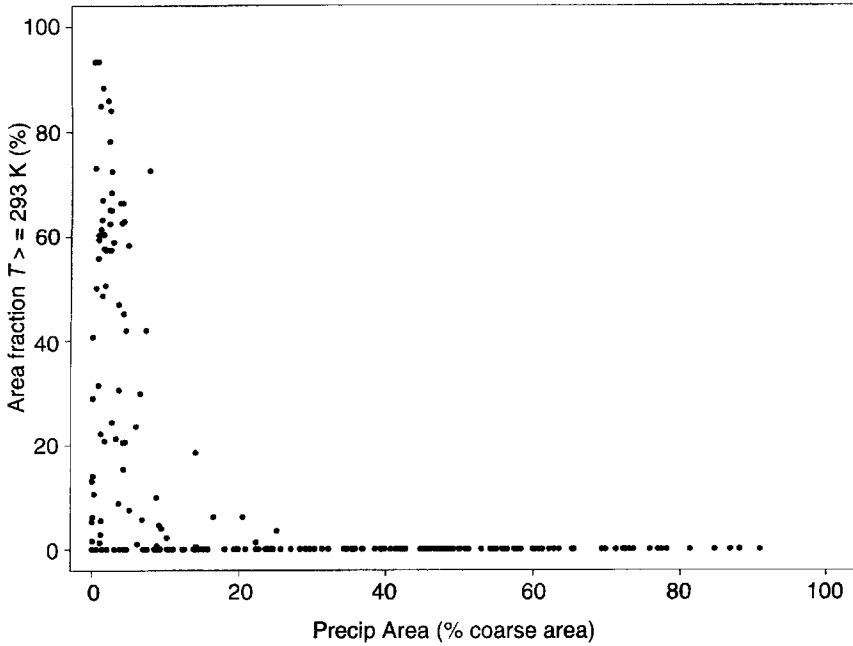
Figure 13. Scatter plot of precipitation area as percentage of coarse area versus fraction of coarse area with infrared temperature >293 K (nearly clear air).

TABLE 4. PRECIPITATION STRUCTURE AND INFRARED (IR) TEMPERATURE STATISTICS FOR COARSE-RESOLUTION DATA SHOWN IN FIGS. 14 AND 15

Date (UTC)	Time (UTC)	Mean IR temperature (K)	Precipitation area (% of coarse grid)	Convective area (% of coarse grid)	Stratiform area (% of coarse grid)	Stratiform area fraction (% of precipitation area)	'Clear air' fraction		
							>293 K	<238 K	<208 K
13 December 1992	1555	200.1	63.5	0.4	63.1	99	0	0.97	0.81
21 February 1993	0036	225.5	34	2	32	95	0	0.82	0.08
27 November 1992	0548	244.6	12	1	11	95	0	0.4	0
10 January 1993	0048	294.3	2	0.5	1.5	74	0.86	0	0

details of the full IR temperature distribution over a coarse area, histograms of GMS IR temperature with a bin size of 5 K were constructed for each quality-controlled coarse area. Some examples of these IR temperature histograms for individual coarse areas and the associated CS maps of the underlying precipitation are described in Figs. 14 and 15 and statistics given in Table 4. Figure 14(a) shows a narrow distribution of temperatures centred around a very low mean value of 200.1 K. The associated underlying precipitation (Fig. 15(a)) is widespread and covers 63% of the coarse area and is 99% stratiform by area. Figures 14(b) and 15(b) show a case of widespread precipitation, at a later stage of storm evolution than in (a); the precipitation is 95% stratiform by area and has a wide distribution of IR temperature values with a mean value of 226.1 K. Chen and Houze (1997) noted that intermediate values of IR temperature are often associated with the later stages of tracked cloud clusters. Figures 14(c) and 15(c) show a wide distribution of IR temperature
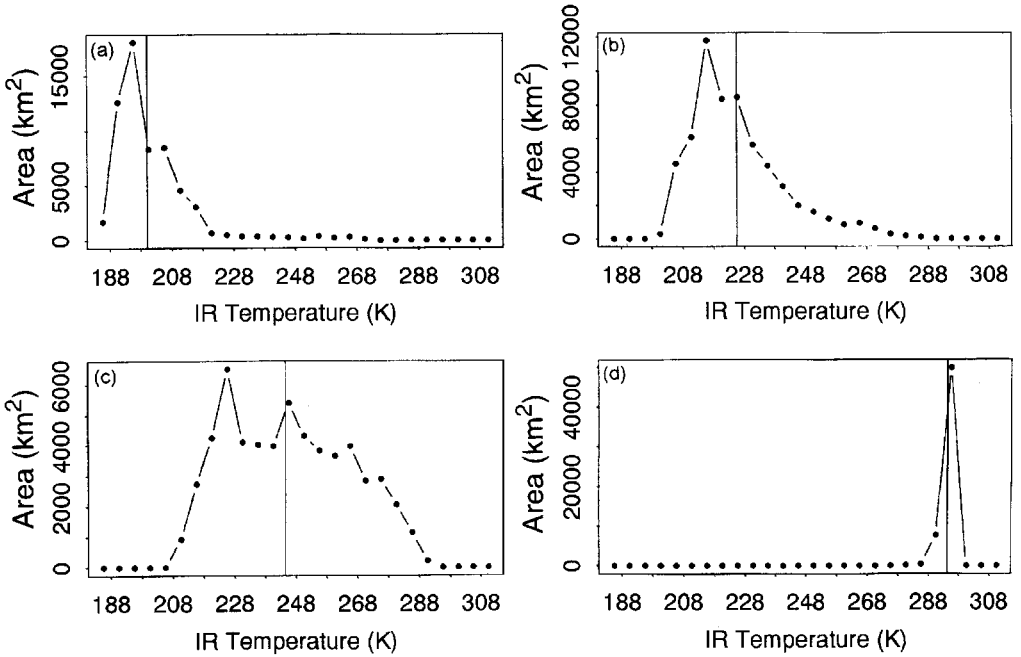
Figure 14.   Infrared (IR) temperature for selected coarse resolution samples: (a) 1555–1600 UTC 13 December 1992, (b) 0036–0041 UTC 21 February 1993, (c) 0548–0553 UTC 27 November 1992, and (d) 0048–0053 UTC 10 January 1993. Vertical lines indicate mean IR temperatures over the coarse area (also see Table 4).

associated with spatially dispersed precipitation regions that cover 12% of a coarse area. Figures 14(d) and 15(d) show an extremely narrow IR temperature distribution centred around a very high mean IR temperature of 294.4 K associated with a spotty pattern of precipitation covering only 2% of a coarse area.

In Fig. 16 all the IR histograms, like those in Fig. 14, are plotted in the same graph. Each histogram is represented by a vertical strip of grey shading, with darker shades indicating higher frequencies. For clarity of presentation, only those histogram bins containing >5% of a coarse area are shown. The histograms are sorted from left to right by increasing mean IR temperature over a coarse area. Heavy dots show the value of the mean IR temperature for each histogram. Arrows in Fig. 16 show the locations of the four example histograms in Fig. 14. Figure 16 allows us to see and compare the IR histograms from each coarse-resolution sample at once. The distribution of IR temperature is narrowest (~10–30 K) when the mean IR temperature is very high (>292 K) and very low (<208 K). At mean IR temperatures between these extremes the distribution is wider (~50–90 K). These trends in the width of the IR temperature distribution are similar to those shown by Fig. 2 of Fu *et al.* (1990). Although only a rough measure of the full distribution, mean IR temperature is usually near the centre of the distribution and has sufficient dynamic range to represent the full range of observed variation.

In Fig. 17 all the coarse-area IR histograms are plotted in the same graph, as in Fig. 16. However, in Fig. 17 the histograms are sorted from left to right by increasing size of the precipitation area (as a percentage of a coarse area), and heavy dots show the size of the precipitation area. For precipitation areas <10% of a coarse area, the mode of the IR temperature distribution is at a very high temperature, ~295 K. Coarse areas containing precipitation regions with sizes between 10–25% of a coarse area have a wide multi-
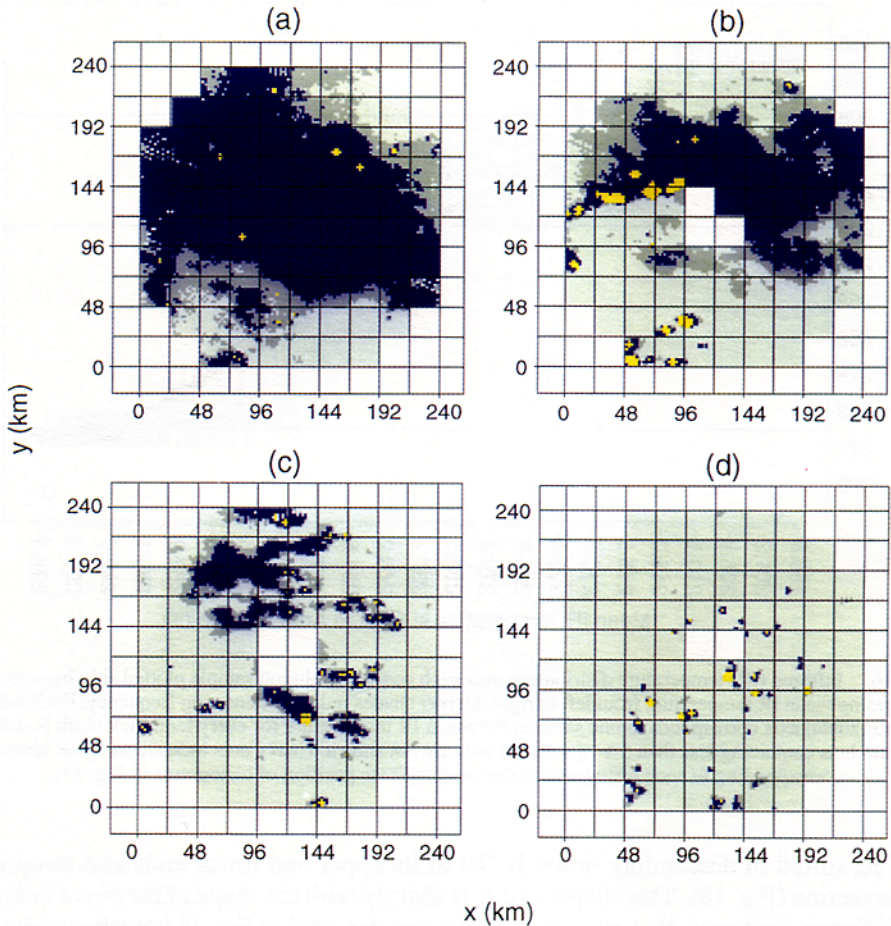
Figure 15. Convective/stratiform (CS) maps for coarse areas corresponding to histograms in Fig. 14. CS map colour definitions as in Fig. 5.

modal IR temperature distribution with individual modes at values between 215–295 K. Precipitation areas between 25–60% of a coarse area also exhibit a wide IR temperature distribution but with a mode near 215 K. When the precipitation area is >60% of a coarse area, the IR temperature distribution narrows and has a single mode between 185–210 K. The largest precipitation areas are associated with IR temperature distribution modes at the lowest temperatures. The complexity of the pattern of the frequency distribution of IR temperature in the histograms of IR temperature for individual coarse-area samples sorted by precipitation-area size in Fig. 17 is an indication that no simple statistic of the IR temperature distribution correlates well with precipitation area.

(ii)   *Mean IR temperature versus area fraction* <238 K. A popular method for representing satellite data is 'per cent high cloudiness' (Arkin and Meisner 1987; Chen *et al.* 1996), which is usually defined as the fraction of an area occupied by IR temperature pixels with values less than some threshold (usually ∼238 K). This parameter of the IR temperature distribution over the area may behave differently than the mean IR temperature over the area. To check this difference, in Fig. 18 we plot the coarse-area IR histograms in Fig. 16, except that the histograms are sorted by area fraction <238 K. The curve of area fraction
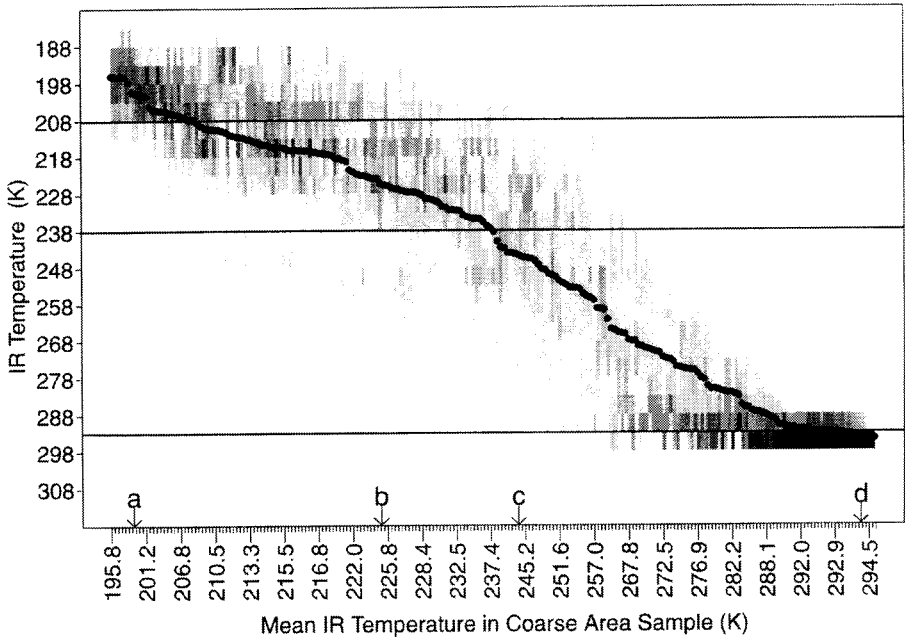
Figure 16.   Infrared (IR) temperature distribution over each coarse-resolution sample plotted side-by-side, sorted by increasing mean IR temperature from left to right. Darker shades indicate increasing frequency. Each tick mark on the horizontal axis corresponds to one sample; the mean IR temperature for every tenth tick mark is indicated. Histogram bins containing less than 5% of a coarse area are not shown. Heavy dots indicate mean IR temperature corresponding to each histogram. Letters a–d indicate position of histograms in Fig. 14.

<238 K, sorted in descending order, is flat at its upper and lower ends and steep in the middle section (Fig. 18). This shape contrasts sharply with the shape of the curve in Fig. 16. This difference indicates that mean IR temperature depicted in Fig. 16 has a better dynamic range, i.e. it is likely to be a better proxy for a related variable such as precipitation area. To test this idea we compare the joint-probability distribution of mean IR temperature and precipitation area (Fig. 19(a)) with the joint-probability distribution of the per cent of each coarse area sampled by the aircraft that was covered by pixels with IR temperature <238 K and precipitation area (Fig. 19(b)). At coarse resolution, the data representing area fraction <238 K (per cent high cloudiness) versus precipitation-area size are more widely scattered than those of mean IR temperature versus precipitation-area size (Fig. 19).

In choosing variables for the joint-probability distributions, sets of variables whose joint distribution is tighter are preferred to those whose distribution is wider and thus more random (Packard *et al.* 1980). Thus we will use mean IR temperature to represent the characteristics of the IR temperature distribution over a coarse area.

(c)   Total precipitation area over a coarse area

The correlation between decreasing coarse-resolution mean IR temperature and increasing precipitation-area size (Fig. 19(a)) is extremely weak (correlation coefficient = 0.05). However, the population of points is nonetheless limited to a subset of the possible variable space rather than being randomly distributed. This is like a phase space representation of a nonlinear dynamical system in that it shows the physically feasible combinations without assuming a linear correlation. To aid in characterizing the joint-probability distribution, the data in Fig. 19(a) are subdivided into three panels containing
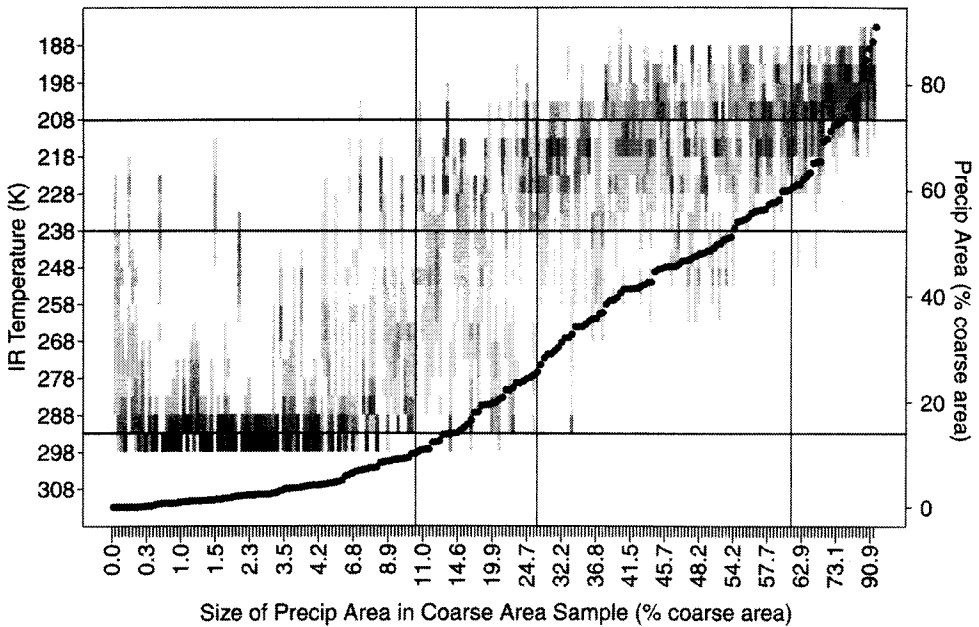
Figure 17.   Infrared (IR) temperature distribution over each coarse-resolution sample plotted side-by-side, sorted by increasing precipitation area from left to right. Darker shades indicate increasing frequency. Each tick mark on the horizontal axis corresponds to one sample; the fractional size of the precipitation area (% coarse area) for every tenth tick mark is indicated. Histogram bins containing less than 5% of a coarse area are not shown. Heavy dots indicate size of precipitation area corresponding to the IR temperature histogram for each coarse area. Precipitation-area size (heavy dots) is overlaid.
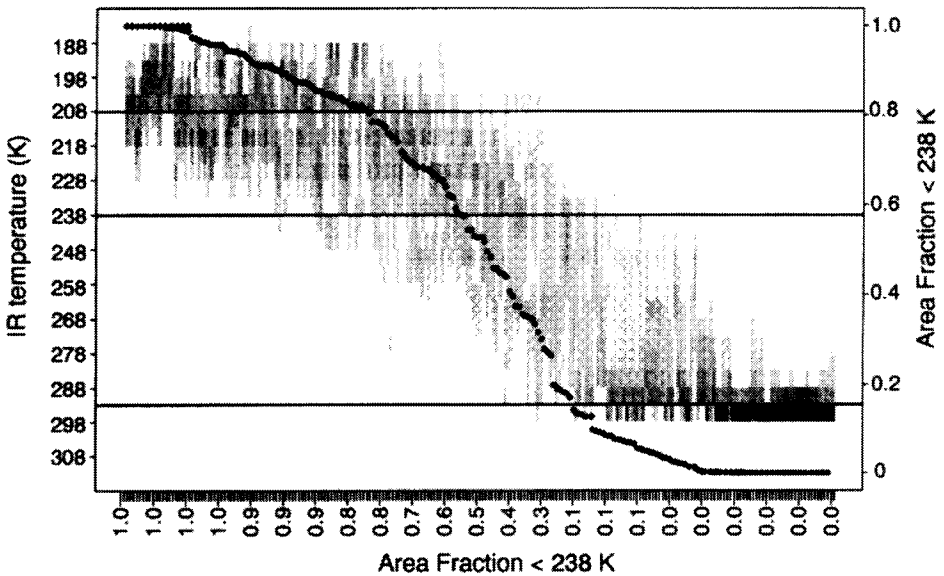

Figure 18.   As in Fig. 16, except IR temperature distribution over each coarse-resolution sample plotted side-by-side and sorted by decreasing area fraction <238 K from left to right. Each tick mark on the horizontal axis corresponds to one sample; the area fraction <238 K for every tenth tick mark is indicated. Heavy dots indicate area fraction <238 K corresponding to each histogram.
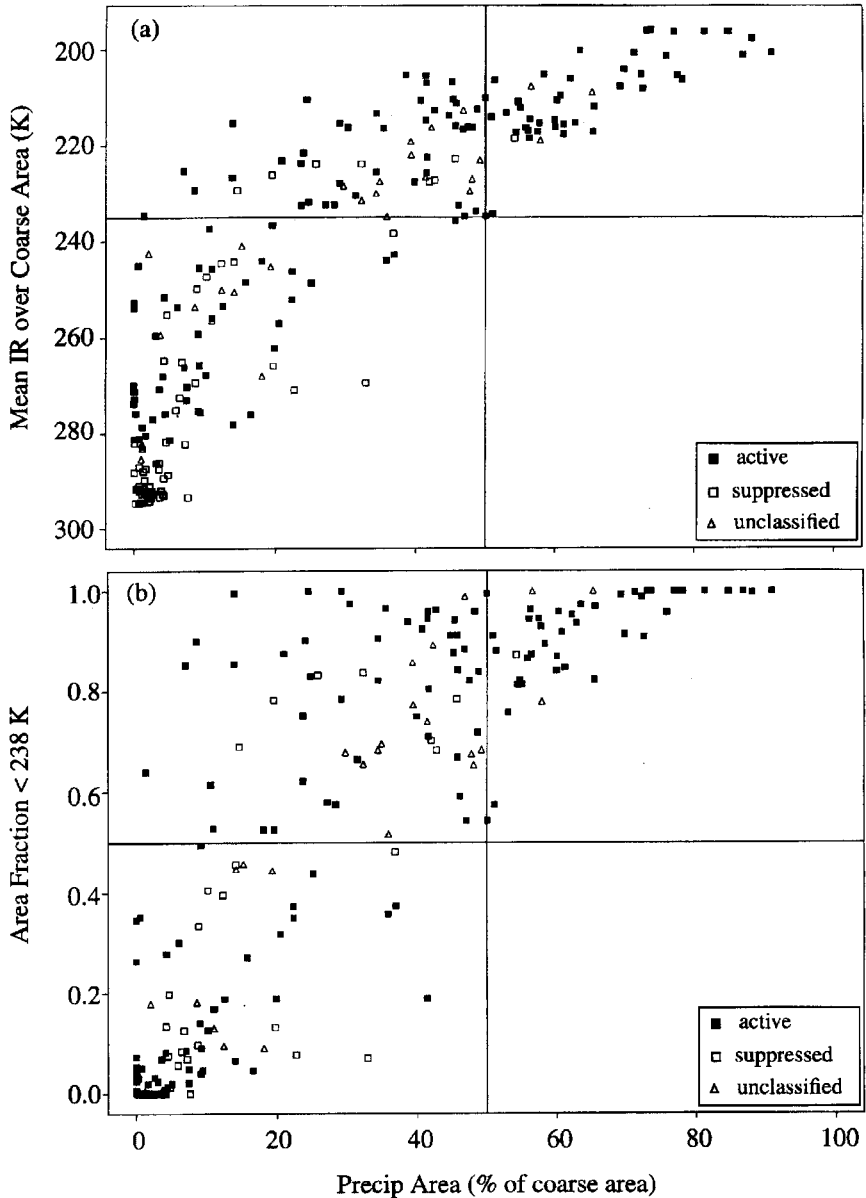
Figure 19. Scatter plots of total precipitation area versus (a) mean infrared (IR) temperature and (b) area fraction <238 K at coarse resolution. See text for explanation of the symbols.

the points for active, suppressed, and unclassified periods in Fig. 20, and each panel of the figure is divided into four quadrants defined by a horizontal line at 235 K and a vertical line at a precipitation-area size of 50% of a coarse area. These lines aid in showing that when the mean cloud-top temperature over a coarse area is >235 K, the precipitation area never exceeds 50% of a coarse area (lower-right quadrant is empty), and seldom exceeds 30% (lower-left quadrant). *High mean cloud-top temperature over a coarse area thus implies a small area of precipitation.* When the area covered by precipitation is >50%, the mean cloud-top temperature over a coarse area is very low, generally <225 K (upper-right quad-
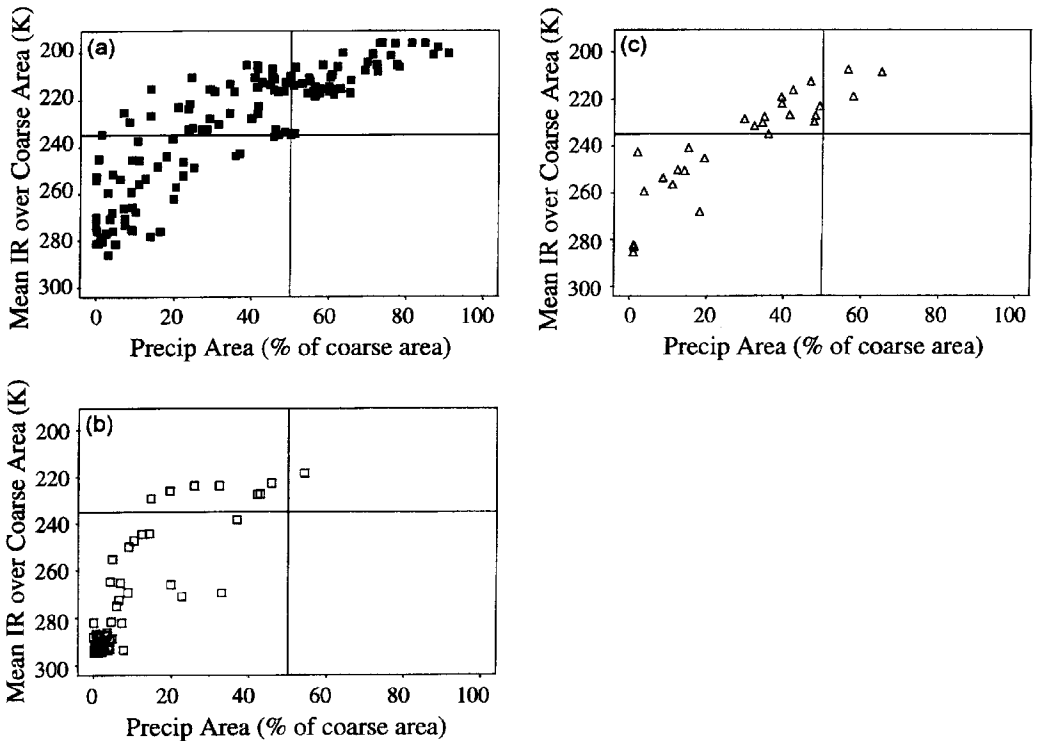
Figure 20.   Scatter plots of total precipitation-area coverage versus mean infrared (IR) temperature at coarse resolution. Samples from the (a) active phase, (b) suppressed phase, and (c) unclassified phase of the intraseasonal oscillation (see text).

rant). Thus, *a large rain area implies a very low mean cloud-top temperature at coarse resolution. But the converses are not true*: low mean IR temperature (<235 K) can be associated with rain areas of any size (0–90% of the coarse area according to Fig. 19(a)); and small rain areas (<20% of the coarse area) can be associated with almost the entire range of mean IR temperature observed over the coarse area (215–295 K according to Fig. 19(a)).

These rules apply under active, suppressed and unclassified conditions alike. However, under suppressed conditions, mean cloud-top temperatures <235 K over a coarse area seldom occur (left and right upper quadrants of Fig. 20(b)) and cloud-top temperature is never <220 K. The division into active, suppressed and unclassified phases of the ISO represents different sets of environmental conditions in which precipitating cloud systems exist. For economy of presentation, the three categories will be combined in later figures.

(d)   Convective precipitation area at coarse resolution

The area covered by convective precipitation is always small (<10% of a coarse area, Fig. 21). Similar to the results at fine resolution, the area covered by convective precipitation is roughly independent of IR temperature, except when the mean cloud-top temperature is very low (<220 K). The range of area coverage of convective precipitation may be partly indicative of the stage of evolution of the storm. Since the fine-resolution results do not show a dependence of area of convective activity on IR temperature, *the larger areas of convective precipitation at coarse resolution at very low temperatures*
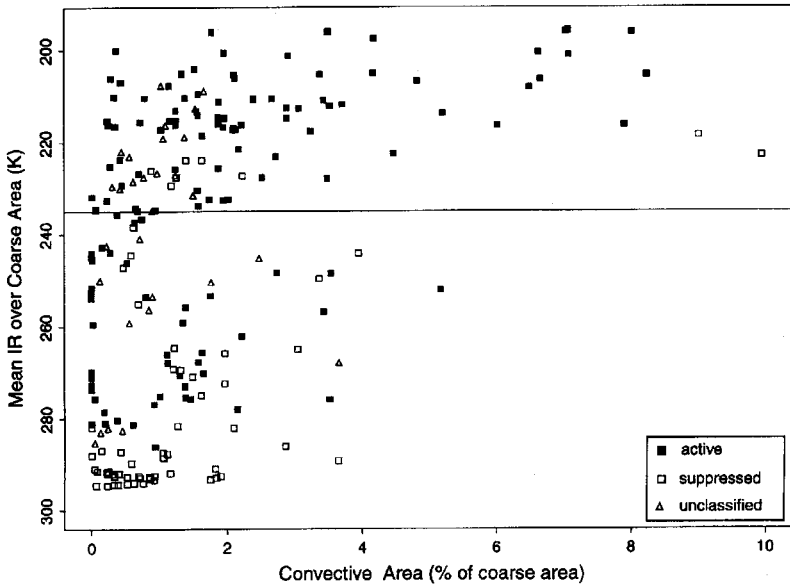
Figure 21.   Scatter plot of convective precipitation area versus mean infrared (IR) temperature at coarse resolution. Points coded by active suppressed/unclassified phase (see text) of the intraseasonal oscillation. Horizontal line marks 235 K.

(upper right of Fig. 21) *indicate small convective cells dispersed over a large area within the precipitation region rather than contiguous convective activity concentrated in one spot.*

(e)   *Stratiform precipitation area at coarse resolution*

The relation between stratiform precipitation area and IR temperature at coarse resolution (Fig. 22) is similar to that of precipitation as a whole (Fig. 19). As was true for precipitation structure in the tropical eastern Atlantic observed during GATE* (Houze and Cheng 1977), the area of convective precipitation does not vary much from storm to storm and thus the area of the overall precipitation region reflects the size of the stratiform region.

(f)   *Convective area versus stratiform area*

A scatter plot of convective area versus stratiform precipitation area at coarse resolution is shown in Fig. 23. There is *no clear relation between the instantaneous areas of stratiform precipitation and convective precipitation.* The size of the convective region is constrained over a narrow range from 0 to 5000 km². This range of values is likely, at least partly, to be related to the stage of storm evolution. Life cycle cannot be directly addressed with the data in this study. However, since convective activity is dispersed (section 5(a)) and larger convective areas are not instantaneously associated with larger stratiform areas, environments that can sustain this dispersed convective activity for longer periods must account for larger precipitation regions. Over a period of sustained convective cell activity, as each cell weakens it evolves into stratiform precipitation (as discussed in section 3(a)), with a longer lifetime than a convective cell, and the size of the stratiform region grows as each cell finishes its active convective phase and is added to the stratiform area. Future

* GARP (Global Atmospheric Research Program) Atlantic Tropical Experiment.

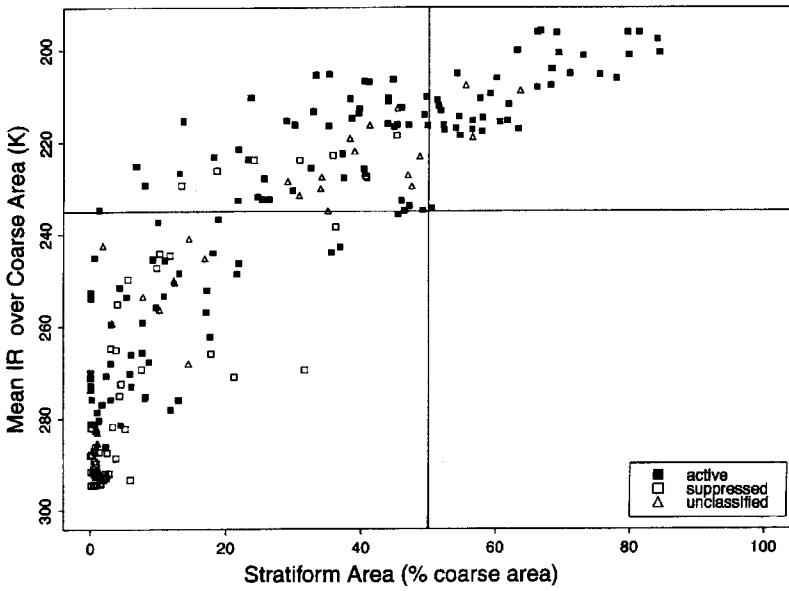Figure 22. As Fig. 21 but for stratiform precipitation area versus mean IR temperature at coarse resolution.
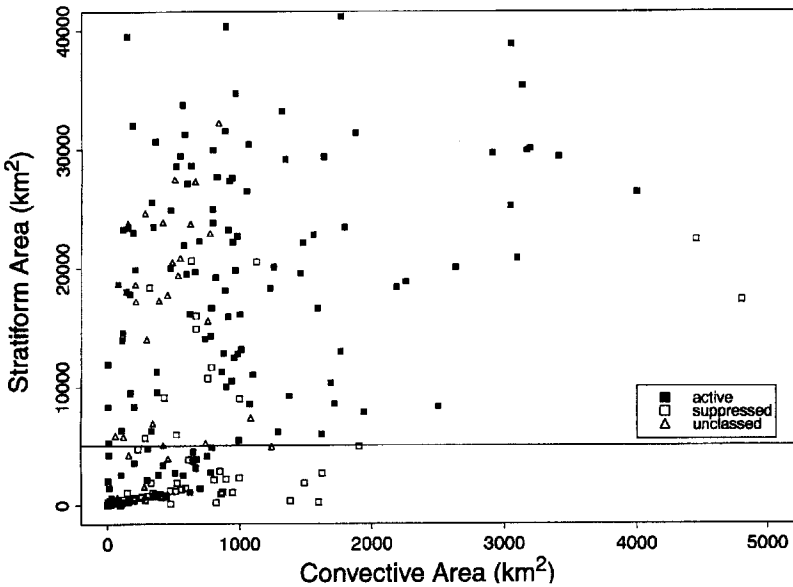

Figure 23. Area of convective precipitation versus area of stratiform precipitation at coarse resolution. Points coded by active/suppressed/unclassified phase (see text) of the intraseasonal oscillation. Horizontal line at 5000 km^2 (maximum convective-precipitation area in x axis).
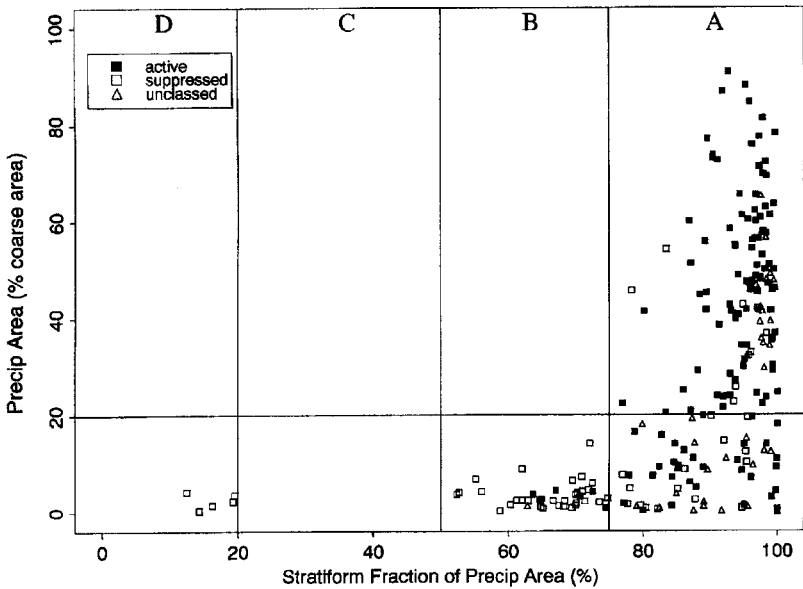
Figure 24. Stratiform area fraction of total precipitation area versus size of precipitation area at coarse resolution. Points coded by active/suppressed/unclassified phase (see text) of the intraseasonal oscillation. See text for discussion of regions A–D.

studies should therefore examine the *time-integrated area* of convective precipitation and its relation to the eventual size of the stratiform region.

(g)   Coarse resolution convective and stratiform precipitation ratios

(i)   *Area.* The ratio of the stratiform precipitation area to the total precipitation area indicates the relative importance of stratiform precipitation without the assumptions inherent in applying rain rates. We have divided the scatter plot of stratiform fraction of total precipitation area (Fig. 24) into four regions: (A) precipitation regions >75% stratiform by area—these systems encompass the full range of sizes; (B) precipitation regions 50–75% stratiform by area—these are confined to small systems <20% of a coarse area; (C) systems of 20–50% stratiform area fraction, which were infrequent enough not to be sampled by aircraft; and (D) five samples with <20% stratiform area corresponding to early, mature and decaying stages of convective activity sampled on 28 November 1992, in a warm cloud system whose radar echoes did not extend above the 0 °C level. Thus, precipitating regions of cold clouds (containing ice) with more than 50% convective precipitation by area were not sampled, and most had <25% of their area consisting of convective regions. This characteristic of the joint-probability distribution is likely related to the virtually 100% probability of stratiform precipitation within precipitating fine-grid elements with mean cloud-top temperature less than 273 K (Fig. 11). As in the GATE, extremely small, individual precipitating regions ($<10^3$ km^2) could be almost completely composed of convective precipitation (Cheng and Houze 1979). However, such regions rarely occur in isolation. It is the ensemble of these extremely small regions in various stages of their life cycle over a coarse area, and over extended periods of time, that combine to produce the statistic of a minimum 50% stratiform fraction for cold clouds.

(ii)   *Rainfall.* The fraction of stratiform rainfall accumulated over a month, or the several weeks of a field project, is commonly used to characterize precipitation structure. Time-integrated stratiform fractions are usually between 40–60% in tropical precipitation (Houze 1977; Cheng and Houze 1979; Gamache and Houze 1983; Leary 1984; Churchill and Houze 1984; Houze and Rappaport 1984; Houze and Wei 1987; Chong and Hauser 1989; Steiner *et al.* 1995). We will examine the stratiform rainfall fraction as a function of mean cloud-top IR temperature and precipitation region area.

The relative amounts of convective and stratiform precipitation are obtained by weighting the convective and stratiform areas by an areal average conditional rain-rate ratio of 3:1. This ratio is based on the derived areal average stratiform conditional rain rate of 3.9 mm h^{-1} and a lower bound for the areal average conditional convective rain rate of 10.0 mm h^{-1} from TOGA COARE aircraft particle-probe data (Yuter and Houze 1997). Since the aircraft radar data set oversampled cold cloud conditions and is overall wetter than a climatological sample (Fig. 2), application of conditional area rain rates will yield an *upper bound* on the climatological stratiform fraction of rain and daily rainfall. The resulting stratiform rain fraction is 84%, reflecting the larger number of large precipitation systems in this sample compared with their climatological frequency. There is also a bias in the aircraft sample toward precipitation systems in their mid-to-late stages of development. This bias is a result of nearly always flying the aircraft toward a pre-existing mesoscale system.

The wide vertical beam width and uncalibrated nature of the LF radar makes derivation of rainfall directly from reflectivity values untenable. The area-integrated rain rate for each coarse area is estimated using

$$\mathfrak{R}_{\text{area}} = R_{\text{cc}} A_{\text{cc}} + R_{\text{s}} A_{\text{s}} \tag{2}$$

where $\mathfrak{R}_{\text{area}}$ is the total volume of rain falling per unit time over the total coarse area (convective, stratiform and non-raining areas), R_{cc} is the area-average rain rate in convective regions, R_{s} is the area-average rain rate in stratiform regions, A_{cc} is the area of convective precipitation, and A_{s} is the area of stratiform precipitation. This method is similar in spirit to those that use a mean rain rate to represent rainfall over a large area (Doneaud *et al.* 1984; Arkin and Meisner 1987). As a test of the consistency of the conditional average rain-rate values, Eq. (2) was applied to the 221 CS maps using a conditional area-average stratiform rain rate of 4 mm h^{-1} and a conditional area-average convective rain rate of 12 mm h^{-1}. The resulting average area-integrated rainfall for the aircraft radar-sampled coarse areas is 1.2 mm h^{-1} (29 mm day^{-1}) using an assumption that each map is valid for 1 hour.* Application of the convective and stratiform conditional rain rates to the ISO active and suppressed phase subsets of the aircraft sample yields average area-integrated rainfall rates over a coarse area of 1.6 mm h^{-1} and 0.47 mm h^{-1} respectively. Since the aircraft often targeted actively precipitating regions, these aircraft sample rainfall rates will be much greater than rainfall calculations over any one fixed area. Indeed, the rainfall rate of 29 mm day^{-1} for the aircraft radar sample is much higher than the mean precipitation calculations over the entire IFA during the IOP of 6.31 mm day^{-1} from the Microwave Sounder Unit data, 6.62 mm day^{-1} from the Special Sensor Microwave Imager/I data (Brown 1994), and $\sim$7 mm day^{-1} obtained from preliminary analysis of sounding data (R. Johnson (1996), personal communication). It is also much wetter than the 5.4 mm day^{-1} average rain rate observed in the eastern part of the IFA by the shipborne radars (Short *et al.*, personal communication). Since there was a higher relative frequency of cold cloud

---

* A time integration of 1 hour corresponds to the sampling necessary to obtain monthly rainfall accumulation uncertainty of less than 10% (Steiner *et al.* 1995).
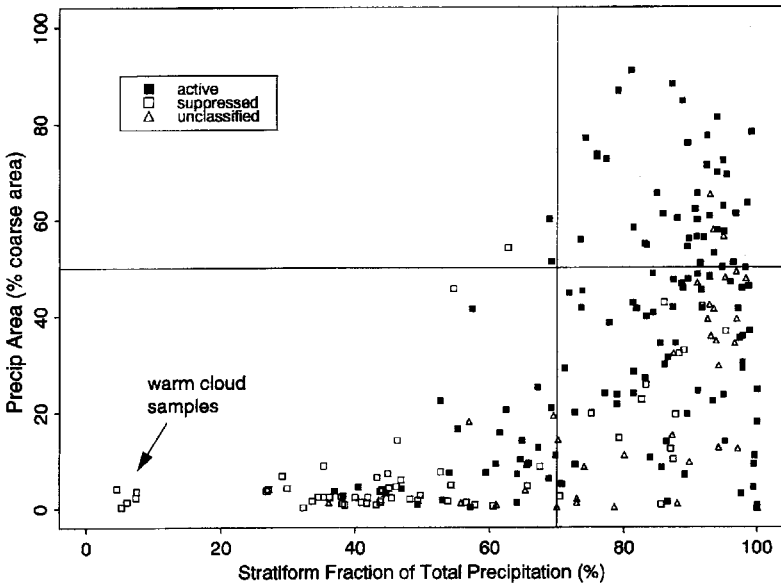
Figure 25. Stratiform rain flux fraction of total precipitation flux versus size of precipitation area at coarse resolution. Points coded by active/suppressed/unclassified phase (see text) of the intraseasonal oscillation.

tops and lower relative frequency of warmer cloud tops in the aircraft sample compared with the ship samples over the IFA (Figs. 2(b) and (c)), the daily average rain rates are not directly comparable. However, the average rain rates from the airborne sample can be used as upper bounds on estimates calculated for the four-month period over the IFA and TOGA COARE domains.

Since estimation of stratiform rain fraction requires approximating rain rates within convective and stratiform regions, calculation of stratiform rain fraction will have a larger margin of error than that of stratiform area fraction. However, despite the greater uncertainty, stratiform rain fraction provides important information on the relative contributions of stratiform and convective regions to the integrated diabatic heating produced by a precipitation region. Figures 25 and 26 show the relations between the stratiform rain fraction of total precipitation to precipitation-area size and mean IR temperature at coarse resolution, respectively. In general, the weak association between mean IR temperature and precipitation area (Fig. 20) acts to spread points in Fig. 26 compared with Fig. 25.

Larger precipitation areas >20% of a coarse area usually had a stratiform rain fraction >70% (Fig. 25). Smaller precipitation areas <20% of a coarse area exhibit a wide range of stratiform rain fractions with the smaller stratiform rain fractions (<60%) tending to occur during the suppressed phase of the ISO (Fig. 25). Points with nearly 100% stratiform rain fraction at all precipitation-region sizes reflect precipitating regions that were sampled near the end of their life cycle when they were almost entirely stratiform in character. The five suppressed points with <10% stratiform rain fraction in Figs. 25 and 26 are the samples from warm clouds (entirely below the 0 °C level) discussed in section 5(g)(i).

Figure 26 is broken into three panels to show the distribution of data occurring within the active, suppressed and unclassified phases of the ISO more clearly. The low mean IR temperature samples (<235 K) which occurred primarily during the active phase of the ISO were usually >70% stratiform by rain fraction (Fig. 26(a)). From Fig. 20 we know that these low mean IR temperature samples are associated with a range of precipitation-region sizes; Figs. 25 and 26 reveal that those active phase samples with stratiform rain fractions >70%,
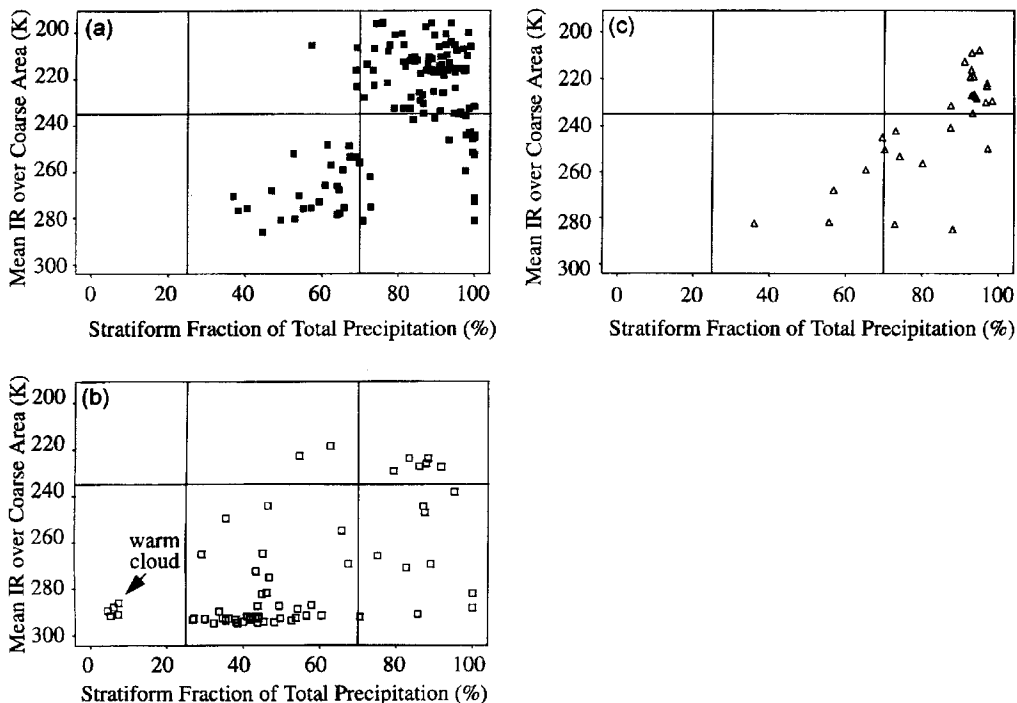
Figure 26. Stratiform fraction of total precipitation versus mean infrared (IR) temperature at coarse resolution. Samples from the (a) active phase, (b) suppressed phase, and (c) unclassified phase (see text) of the intraseasonal oscillation.

although clustered at <235 K mean IR temperature, are associated with precipitation areas whose sizes range from near 0 to 90% of the coarse area. The suppressed phase samples from clouds containing ice (e.g. cold clouds) exhibit a wider range of stratiform rain fractions (Fig. 26(b)). Most of the samples at mean IR temperatures >280 K over a coarse area are from the suppressed phase of the ISO, and have small precipitation areas <10% of a coarse area (Fig. 20). These samples usually exhibit stratiform rain fractions from 25 to 60% (Fig. 26(b)). As in Fig. 20(c), the distribution of unclassified points in Fig. 26(c), tends to occur in regions of joint-probability space where both active and suppressed points are distributed as well. Thus, the colder cloud systems (mean temperatures <235 K over a coarse area) occurring during the active phase of the ISO produced >70% of their rain within stratiform regions, *independent* of precipitation-region size. The warmer, smaller systems occurring during the suppressed phase of the ISO usually had a smaller percentage of stratiform rain.

6. RELATION OF PRECIPITATION STRUCTURE TO ENVIRONMENT

(a) Synoptic

Since the size of the stratiform region determines the overall size of the precipitation area, the data previously shown in Fig. 22 are categorized by synoptic-scale surface wind direction (Table 2) and shown in Fig. 27. Under northerly and calm surface winds, only small precipitation regions associated with higher mean IR temperatures (>260 K) were sampled (Fig. 27(c)). However, small precipitation systems can occur under all wind directions. Large, cold systems with stratiform area >50% of a coarse area and mean IR
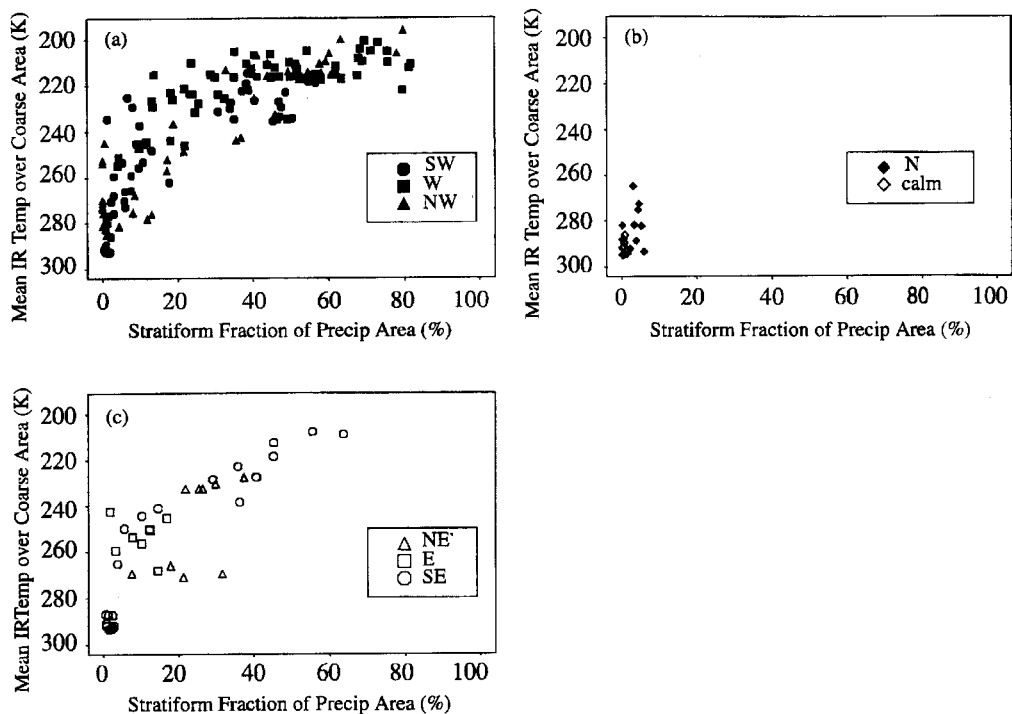
Figure 27.   Scatter plots of stratiform area fraction of precipitation region versus mean infrared (IR) temperature
at coarse resolution. Points coded by surface synoptic-scale wind directions (see Table 2).

temperature <220 K over a coarse area occur almost exclusively under westerly conditions (Fig. 27(a)). Except for these associations, wind direction in itself does not appear to have any relationship to the size of the precipitation area. For example, westerly and easterly winds are associated with almost the entire range of sizes of stratiform precipitation area (Figs. 27(a) and (b)).

(b)   Basic inflow-sounding parameters

To investigate further the relationship between precipitation-area size and some basic kinematic and thermodynamic parameters, mission averages of sampled precipitation characteristics were compared with inflow-sounding layer averages for 500–1000 m and 5000–5500 m above mean sea level of wind direction, wind speed, temperature and cloud liquid-water content (Table 3). Kingsmill and Houze (1995) used LF radar composites and flight-level winds to determine which ascent and descent soundings of the NCAR Electra and the two NOAA WP-3D aircraft performed during a mission were obtained within environmental air flowing toward the storm. These *in situ* measurements were combined with the closest Integrated Sounding System (ISS) sounding to obtain a thermodynamic profile of the inflow environment. The lowest altitude of the inflow sounding varied from mission to mission, making calculation and comparison of standard indices like low-level shear, convective available potential energy (CAPE) and Richardson number problematic. However, previous studies have shown that CAPE varies only slightly from storm to storm over the western Pacific (Mapes 1993; Brown 1994). We restrict our analysis to a few basic measured quantities that were available from the 18 NOAA WP-3D missions where the inflow environment was sampled. To aid in placing the mission-to-mission sampling in a

relative context, the mission average precipitation-area coverage and the mission average sizes of the convective and stratiform portions of the total precipitation area are indicated in Table 3. Although these indicators are a function of the nature of the storm, its life-cycle stage, and the sampling of the storm by the aircraft, they are useful as a crude measure of the overall characteristics of the storm.

Analysis of the inflow-sounding-measured layer averages for 500–1000 m and 5000–5500 m versus the size of the precipitation area *does not yield significant correlations between the sizes of precipitation region and layer averages of wind direction, wind speed, temperature or liquid-water content from the inflow soundings* in this sample of 18 NOAA WP-3D missions. While weak low-level winds are associated with smaller precipitation areas, both large and small precipitation areas are associated with strong low-level winds (Figs. 28(a) and (b)). The association of a wide range of convective activity with stronger magnitude surface winds is also evident from Zhang's (1996) analysis of three years of western Pacific Tropical Atmosphere Ocean (TAO) buoy observations, and Lin and Johnson's (1996) analysis of sounding and satellite data from the TOGA COARE IFA.

Raymond (1995) used mean IR temperature as a proxy for convective activity, and showed an apparent relationship between Electra near-surface flight-level wind speed and GMS satellite IR temperature averaged over $2° \times 2°$ areas (approximately the size of our coarse areas). Raymond's methodology does not distinguish between the inflow air feeding the updraughts and air that has been processed through the storm. Even so, comparison of data from missions with average coarse-resolution IR temperatures less than and greater than 235 K (Figs. 28(c) and (d)) show a similar relationship for the WP-3D inflow-sounding 500–1000 m layer-average wind speed and mission-average precipitation area. However, there is only a weak correlation (correlation coefficient $= 0.05$, section 5(c), Fig. 19) between decreasing mean IR temperature and increasing size of precipitation area, which is a more direct indication of cloud system intensity (see also further discussion in section 7). The correlation between wind speed and convective activity is more diffuse when viewed in terms of precipitation-area size (Figs. 28(a) and (b)) rather than mean IR temperature (Figs. 28(c) and (d)).

7. THE PHASE-SPACE ATTRACTOR OF PRECIPITATING CLOUDS IN THE TOGA COARE

The variability of convective activity sampled by aircraft radar during the TOGA COARE is not easily categorized. The association of the radar and satellite parameters examined in this study do not form distinct populations or statistically significant correlations, and hence do not lend themselves to representation with simple formulae of regressed parameters. However, the data nonetheless exhibit some order which, if described succinctly, can contribute to an improved understanding of the climatology of convective activity over the western Pacific warm pool.

Although the precipitation structure and IR temperature parameters (representing the cloud structure) do not correlate tightly, their joint variations do tend to occur within certain bounds. This behaviour of the joint-probability distributions suggests a phase-space attractor (Lorenz 1993) representation of the variables describing a system of precipitating clouds. Synoptic-scale surface wind direction, basic inflow-sounding parameters, and other measures of the large-scale flow represent the environment, i.e. conditions external to a precipitating cloud system. The active, suppressed and unclassified ISO phases represent different broad sets of these external conditions. The distribution of states within phase space represents the possible combinations of variables of the precipitating cloud system itself without presuming a linear correlation. The coarse-resolution analysis in previous sections of this paper provides four variables describing basic characteristics of
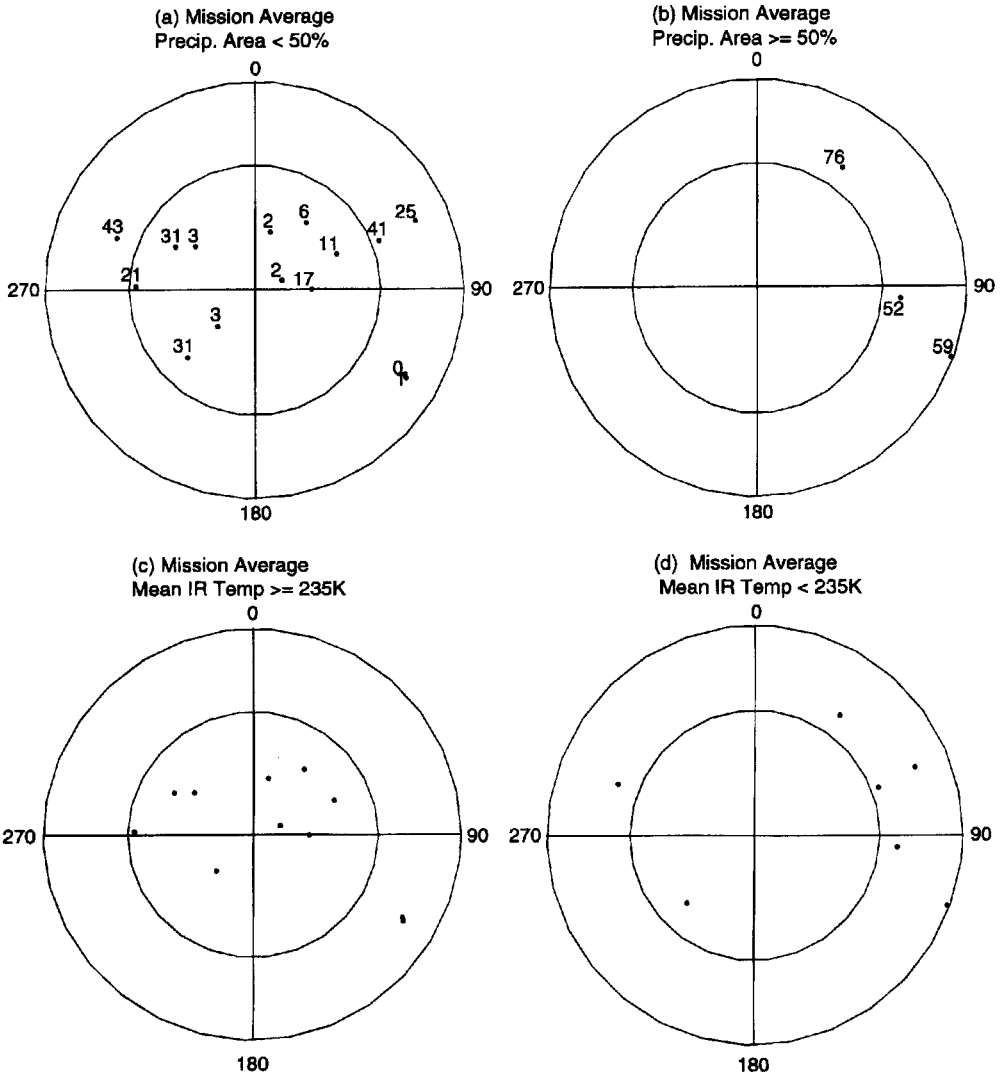
Figure 28.   Mission inflow-sounding layer-average 500–1000 m winds sorted by mission average precipitation-area size and mean infrared (IR) temperature. Points are mapped using the hodograph convention. In each plot the outer radius is at 12 m s^{-1} and the inner circle is at 6 m s^{-1}. Labels in (a) and (b) are mission average precipitation-area size as percentage of a coarse area (Table 2).

the precipitating clouds: the mean IR temperature over a coarse area, the area covered by precipitation, the portion of the precipitation area that is stratiform, and the portion of the area-wide rainfall rate that is stratiform. Figure 29 contains a set of simplified two-dimensional projections of the phase space of these four variables. The phase-space description below pertains to clouds containing ice (cold clouds). True warm clouds were sampled infrequently by the aircraft radar so we have insufficient data to characterize them adequately.

Significant portions of the phase space are empty. Precipitation structures within these empty zones occur so infrequently that they were not sampled by aircraft radar. Since the
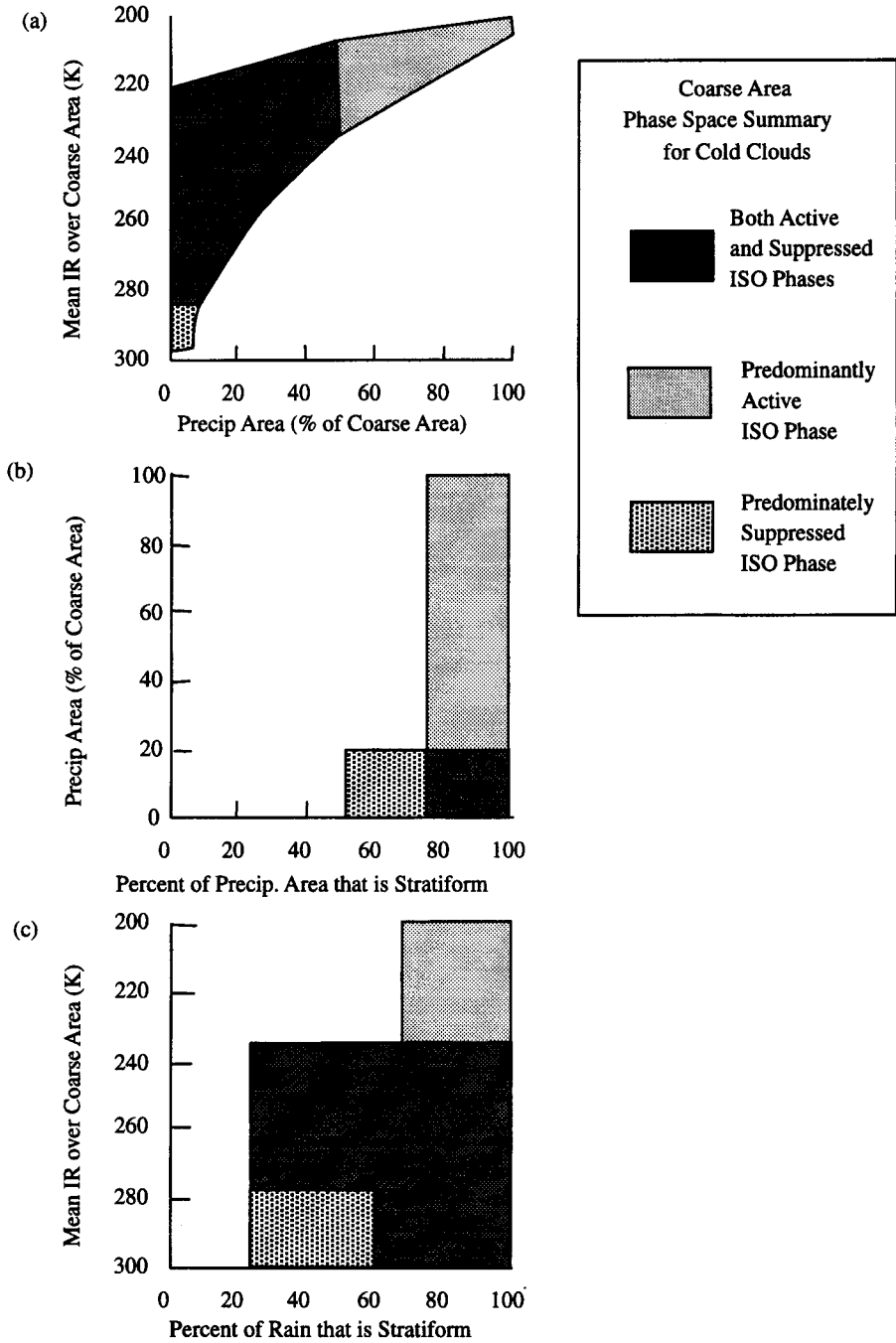
Figure 29. Simplified 2-D projections of *n*-dimensional precipitation structure phase space for cold clouds at coarse resolution (~240 km diameter). (a) precipitation area versus mean infrared (IR) temperature, (b) stratiform area fraction versus precipitation area, and (c) stratiform rain fraction versus mean IR temperature. (See text for explanation of key.)

entire spectrum of convective activity was sampled by the COARE aircraft, it is likely that combinations of parameters within the empty zones are not physically feasible in nature. The remaining portions of the phase space are coded to illustrate the response of the phase space to environmental conditions external to the precipitating cloud systems. We represent three environment sampling categories: predominately active ISO phase samples, predominately suppressed ISO phase samples, or both—containing a mixture of samples from active, suppressed and unclassified phases of the ISO. The distribution of states within the phase-space attractor of the precipitating cloud variables responds to these external environmental conditions.

The simplified projection of the phase-space variables, mean IR temperature over a coarse area and size of precipitation area as a percentage of coarse-area size, is presented in Fig. 29(a). Large precipitation areas have cold cloud tops (IR temperatures <235 K), and they occur predominantly in the active phase of the ISO. Precipitation areas larger than 50% of a coarse area with IR temperatures higher than 235 K did not occur in the data set. Mean IR temperatures >290 K are associated with very small precipitation areas (<10% of a coarse area) occurring in the suppressed phase of the ISO. A large region (shaded area) of the phase space applies in both active and suppressed phases of the ISO and covers a broad range of both precipitation-area size and mean IR temperature. Warmer clouds (mean IR temperature >273 K) have rain areas covering <~20% of a coarse area. Very cold clouds (mean IR temperature 200–235 K) are associated with rain areas covering from 0 to 100% of a coarse area. However, as the mean IR temperature becomes extremely low (<220 K), the probability that the rain area is big (>50% of a coarse area) increases and that it is small (<50%) decreases. Although large regions of the phase space are empty, the breadth of the shaded regions indicates how the mean IR temperature over a coarse area is neither a good index of precipitation-area size nor ISO phase on a case-by-case basis.

The simplified projection of the phase-space variables, precipitation area and stratiform percentage of precipitation area, is shown in Fig. 29(b). This projection relates two precipitation variables, while the other two figure panels relate a cloud property (IR temperature) to a precipitation variable. The empty zones in this plot are much larger than the regions where data samples occurred. There were no samples (of cold cloud) with less than 50% stratiform area. Precipitation areas larger than 20% of a coarse area always have at least 75% stratiform precipitation area. Small precipitation areas, covering <20% of a coarse area, with 50–75% stratiform area, occurred primarily during the suppressed phase of the ISO. Precipitation areas covering 20–100% of a coarse area and >75% stratiform precipitation area occurred primarily during the active phase of the ISO. The distribution of states forming the attractor in this projection of phase space (involving precipitation variables only) is the one showing the strongest distinction between the active and suppressed phases of the ISO.

The relation between coarse-resolution mean IR temperature and stratiform rain fraction is presented in the simplified projection of the phase space in Fig. 29(c). Stratiform rain fractions less than ~70% were *generally* not observed in regions with mean IR temperatures <235 K. Precipitation regions with >70% stratiform rain and temperatures lower than 235 K occurred primarily in the active phase. The combination of mean IR temperature higher than 280 and 25–60% stratiform rain fraction most commonly occurred during the suppressed phase.

The above information from the three graphs can be combined to characterize a particular subset of convective activity: *Larger precipitation areas (>20% of a coarse area) with very cold cloud tops (<235 K mean IR temperature over a coarse area) are >75% stratiform by area, have stratiform rain fractions >70%, and predominately occur in the active phase of the ISO.*

The phase-space attractor description yields a simple method to compare observed and modelled cloud and precipitation structure. Since use of nearly instantaneous, rather than instantaneous, radar and IR temperatures will tend to overestimate the range within phase space occupied by naturally occurring precipitation, model results should fall within the simplified bounds in Fig. 29. The empty spaces within the phase-space plots are regions where model output should not fall.

Although straightforward, the phase-space approach to model verification differs from the approaches often used in verification of models predicting detailed cloud and precipitation structure. We suggest that a mesoscale model that is run to simulate conditions over the warm pool region should be used to generate *statistics* of cloud and precipitation structure over many realizations of convective events. This approach would be the mesoscale analogue to that often employed with GCMs, which verify against statistics of synoptic-scale disturbances and do not attempt to verify synoptic-scale events one-by-one.

8. CONCLUSIONS

The aircraft radar observational programme of the TOGA COARE sampled all parts of the cloud spectrum with a roughly equal number of flight hours. As a result, more samples of the infrequently occurring large cold clouds associated with the active phases of the ISO were obtained by the highly mobile aircraft radars than by the stationary ship radars in the IFA (Fig. 2), and a more robust characterization of this important subset of the cloud spectrum was obtained.

Parameters of radar-echo structure were related to mean satellite-observed IR temperature at two different horizontal resolutions: 24 km × 24 km (fine resolution) similar to mesoscale model resolution, and ~240 km diameter (coarse resolution) similar to global circulation model resolution. The radar echoes were divided into convective and stratiform precipitation areas by means of an objective algorithm applied to 2 km × 2 km resolution C-band radar-reflectivity data from the WP-3D lower-fuselage radar (section 3).

At fine resolution the frequency of occurrence of precipitation increases with decreasing IR temperature (Fig. 10). Mean IR temperatures of 235 K and 208 K correspond to 55% and 88% probability, respectively, of occurrence of precipitation within a fine-grid element. The precipitation region underlying very cold cloud tops always contains stratiform precipitation and has only a 50% probability of containing some amount of convective precipitation (Fig. 11). This result supports the hypothesis that stable adiabatic upward motion within the upper portion of a stratiform cloud shield lowers the cloud-top temperature (Fritsch and Brown 1982; Zipser 1988; Pandya and Durran 1996).

At fine resolution the area covered by precipitation and by stratiform precipitation in particular increases with decreasing mean IR temperature (Fig. 12). In contrast, the area of convective precipitation is essentially independent of mean IR temperature and rarely exceeds 30% (173 km²) of a fine-grid square, indicating a *limit* on the area of convective activity that a given fine-grid volume can support at one time. This result implies a *dispersal* of simultaneous convective activity and seems to justify parametrization of the convective precipitation process on a ~20 km grid scale.

Similar to the results at fine resolution the area of convective precipitation at coarse resolution (240 km diameter) is confined to a relatively narrow size range (<5000 km², Fig. 23) and is also independent of mean IR temperature (Fig. 21). The distribution within this narrow size range is at least partly a function of the stage of storm evolution. The area covered by convective precipitation within a 240 km diameter region at one time is also *independent* of the size of the stratiform precipitation area. The independence of convective precipitation area to mean IR temperature at both fine and coarse scales

implies that *cold cloud top is not an index of convective precipitation. Rather, the area of cold cloud top indicates the area covered by stratiform precipitation.* The limited range of areas of the convective region was also found in radar data from the tropical eastern Atlantic intertropical convergence zone during the GATE (Houze and Cheng 1977). These observations suggest that it is the relative *sustainability* of convective activity over a region (the time-integrated area of convective precipitation) that determines the final size of the area covered by stratiform precipitation, and hence the area of the precipitation region as a whole. Over a period of sustained convective cell activity, the cells never instantaneously occupy more than a small fraction of the coarse area, and never more than 30% of a fine-grid element within the coarse area. However, as each cell weakens it evolves into stratiform precipitation, with a longer lifetime than a convective cell, and the size of the stratiform region grows as each cell finishes its active convective phase and is added to the stratiform area.

The nature of the probability distribution of IR temperature at coarse resolution was investigated. The mean of the distribution has sufficient dynamic range to represent the full range of variation of IR temperature on the coarse scale (Fig. 16). Other measures of the distribution are not as well behaved as the mean IR temperature. Area fraction <238 K does not have as broad a dynamic range and hence it has a poorer correlation with the size of the rain area contained in the coarse region (Fig. 19). The mode of the IR temperature distribution exhibits a jumpy behaviour. For very small precipitation regions (those <10% of the coarse area), the IR temperature distribution mode is near 295 K. The IR temperature distribution tends to be wide and multimodal when the underlying precipitation area is 10–25% of the coarse area, wide with a mode near 215 K when the underlying precipitation area is 25–60% of the coarse area, and narrower and centred near a mode at ∼200 K when the underlying precipitation area is greater than 60% of the coarse area (Fig. 17).

Despite its good dynamic range, *mean IR temperature turns out to be a weak proxy for the size of precipitation areas.* The linear correlation coefficient between decreasing mean IR temperature and increasing precipitation-area size at coarse resolution is 0.05, accounting for less than 1% of the explained variance. Variables of cloud and precipitation structure are better viewed as joint-probability distributions, which, like phase space, identify the physically feasible combinations of variables without presuming a linear correlation.

Analysis of two-dimensional joint-probability distributions of mean IR temperature (a measure of cloud structure) and radar-echo parameters (which measure precipitation structure) on the coarse scale yields insight into the natural variability of precipitation processes over the warm pool.

• Large precipitation areas (>50% of a coarse area) tend to have low mean cloud-top temperatures (<235 K), and high mean cloud-top temperatures (>235 K) are associated with small precipitation areas (<50% of a coarse area). However, *the converse of these two results is not true.* Low mean cloud-top temperatures (<235 K) are associated with a wide range of precipitation areas from near 0% to 90% of a coarse area, and small precipitation areas (<20% of a coarse area) have mean IR temperatures ranging from 210 to 295 K (Fig. 20).

• Ice is an integral part of large cloud clusters. Once precipitation regions reach a critical size (near 20% of a coarse area), the cloud systems are very efficient at spreading ice outside of the boundaries of the precipitation regions (Fig. 13). Large precipitation areas consisting solely of warm clouds (without ice) were not observed (Fig. 20).

• The presence of ice, the size of the rain areas, and the degree to which the precipitation is stratiform are interrelated. Precipitating cold clouds (containing ice) with stratiform area fractions less than 50% were not sampled by the aircraft radar, and may not exist

(Fig. 22). The stratiform fractions of both precipitation area and total rainfall are related to the size of the precipitation region as a whole. Larger rain areas (greater than 20% of a coarse area) are predominately stratiform in area (>75%), while smaller rain areas (<20% of a coarse area) exhibited a wider range of stratiform area fractions from 50 to 100% (Fig. 24). The stratiform rainfall fraction from larger precipitation regions (>20% of a coarse area) is usually over 70% and not less than 50% compared with 5–100% from the smaller precipitation regions (Fig. 25).

The joint-probability distributions reflect the environmental conditions of active and suppressed phases of the ISO. During active phases, the probability that there were no satellite-observable clouds within a coarse-resolution area sampled by aircraft is practically zero (maximum mean IR temperature never >286 K in Fig. 20(a)), while during suppressed phases the near or total absence of clouds is common at coarse resolution (the points cluster near 295 K in Fig. 20(b)). In addition, large rain areas with very cold cloud tops are common under active conditions but do not occur under suppressed conditions (upper-right quadrants of Figs. 20(a) and (b)). This general behaviour of the probability distributions is largely predetermined by our methodology; it is the numerical expression of the a priori definition of active and suppressed time periods in terms of high and low values of per cent high cloudiness at coarse resolution (Chen *et al.* 1996). However, the joint-probability distributions deepen our insight into the differences between active and suppressed conditions. In particular, the large rain areas with very cold cloud tops seen in the active periods are distinguished by large stratiform areas. This result derives purely from the radar observations and thus is not predetermined by the satellite-based definitions of active and suppressed conditions. Stratiform regions during the active phases always constituted more than 60% of the total rain covered area, and any rain area covering 20% or more of a coarse area was 75–100% stratiform by area (Fig. 24). Colder cloud systems (mean temperature <235 K over a coarse area) during the active phase of the ISO produced >70% of their rain within stratiform regions, independent of precipitation-region size (Fig. 26(a)). Stratiform rain fractions varied widely in the suppressed phase since most of the rainfall was associated with small precipitation areas.

Although the joint-probability distributions differ substantially between active and suppressed phases of the ISO, especially in respect to the more robust occurrence of stratiform precipitation during the active phases, the distributions are less sensitive to specific environmental parameters, such as low-level inflow, wind direction, wind speed, temperature and cloud liquid-water content. In particular, the overall precipitation-area size lacked any strong relation to wind speed, wind direction, or thermodynamic variables seen in the storm-inflow soundings obtained by the TOGA COARE aircraft.

The joint-probability representation of the joint variation of precipitation structure and IR temperature over a coarse area is a method of quantifying the wide distribution of observed convective activity observed in the TOGA COARE *without imposing an a priori conceptual model or any subjectively decided structure categories*. This objectivity and generality aids in the application of these results to precipitation structure verification and theoretical studies.

Future work will extend the discussion of the joint-probability distributions in terms of a phase-space attractor of tropical cloud systems by examining the characteristics of tracked regions of contiguous cold cloudiness and relating them to the variables analysed in this study. In this way the snapshots of precipitation structures provided by aircraft can be fitted into the cloud life-cycle context provided by the continuous satellite coverage. However, tracking techniques such as those of Williams and Houze (1987) are themselves dependent on a selected IR temperature threshold, and this dependency must be removed

in a revised tracking method before the phase-space variables of this study can be related meaningfully to the life cycles of objectively tracked cloud systems.

When the coarse-resolution results of this study are summarized in three phase-space diagrams (Fig. 28), one particularly strong result stands out. In the TOGA COARE large precipitation areas (>20% of a coarse grid) with very cold cloud top (<235 K mean IR temperature) are 75% stratiform by area, have stratiform rain fractions >70%, and tend to occur in the active phase of the ISO. Though clear, this result is inexpressible in terms of linear correlations. We therefore suggest that in future studies mesoscale models be run in a manner that is analogous to a GCM. Specifically, a mesoscale model should be run over the time and space domains of the TOGA COARE to generate statistics of the joint variability of mean IR temperatures and precipitation structure (total area covered by rain and stratiform fractions by area and amount). The results of such runs can be verified against the joint-probability distributions of precipitating cloud-system state variables provided by this study. This strategy appears to be the only viable approach to model verification in light of the natural variability of convection over the warm pool.

REFERENCES

Abarbanel, H. D. I., Brown, R., Sidorowich, J. J. and Tsimring, L. S.	1993	The analysis of observed chaotic data in physical systems. *Rev. Mod. Phys.*, **65**, 1331–1392
Adler, R. E. and Negri, A. J.	1988	A satellite infrared technique to estimate tropical convective and stratiform rainfall. *J. Appl. Meteorol.*, **27**, 30–51
Adler, R. E., Markus, M. J., Fenn, D. D., Szejwach, G. and Shenk, W.	1983	Thunderstorm top structure observed by aircraft overflights with an infrared radiometer. *J. Clim. Appl. Meteorol.*, **22**, 579–593
Arkin, P. A.	1979	The relationship between fractional coverage of high cloud and rainfall accumulations during GATE over the β-scale array. *Mon. Weather Rev.*, **107**, 1382–1396
Arkin, P. A. and Meisner, B. M.	1987	The relationship between large-scale convective rainfall and cold cloud over the western hemisphere during 1982–84. *Mon. Weather Rev.*, **115**, 51–74
Bond, G. and Alexander, D.	1994	'TOGA COARE meteorological atlas'. TOGA COARE International Project Office, Boulder, CO, USA
Brown, R. G.	1994	'A modeling and observational study of the convective interaction with large-scale dynamics in the tropics'. Ph.D. thesis, University of Washington
Byers, H. R. and Hall, R. K.	1955	A census of cumulus cloud height versus precipitation in the vicinity of Puerto Rico during the winter and spring of 1953–1954. *J. Meteorol.*, **12**, 176–178

Chen, S. S. and Houze Jr, R. A.   1997   Diurnal variation and lifecycle of deep convective systems over the tropical Pacific warm pool. *Q. J. R. Meteorol. Soc.*, **123**, 357–388

Chen, S. S., Houze Jr, R. A. and Mapes, B. E.   1996   Multiscale variability of deep convection in relation to large-scale circulation in TOGA COARE. *J. Atmos. Sci.*, **53**, 1380–1409

Cheng, C.-P. and Houze Jr, R. A.   1979   The distribution of convective and mesoscale precipitation in GATE radar echo patterns. *Mon. Weather Rev.*, **107**, 1370–1381

Chong, M. and Hauser, D.   1989   A tropical squall line observed during the COPT 81 experiment in West Africa. Part II: Water budget. *Mon. Weather Rev.*, **117**, 728–744

Churchill, D. D. and Houze Jr, R. A.   1984   Development and structure of winter monsoon cloud clusters on 10 December 1978. *J. Atmos. Sci.*, **41**, 933–960

Corbet, J., Mueller, C., Burghart, C., Gould, K. and Granger, G.   1994   Zeb: Software for geophysical data integration, display, and management of diverse environmental data sets. *Bull. Am. Meteorol. Soc.*, **75**, 783–792

Doneaud, A. A., Ionescu-Niscov, S., Priegnitz, D. L. and Smith, P. L.   1984   The area–time integral as an indicator for convective rain volumes. *J. Clim. Appl. Meteorol.*, **23**, 555–561

Emanuel, K. A.   1994   *Atmospheric convection.* Oxford University Press, New York

Fritsch, J. M. and Brown, J. M.   1982   On the generation of convectively driven mesohighs aloft. *Mon. Weather Rev.*, **110**, 1554–1563

Froehling, H., Crutchfield, J. P., Farmer, D., Packard, N. H. and Shaw, R.   1981   On determining the dimension of chaotic flows. *Physica*, **3D**, 605–617

Fu, R., Del Genio, A. D. and Rossow, W. B.   1990   Behavior of deep convective clouds in the tropical Pacific deduced from ISCCP radiances. *J. Climate*, **3**, 1129–1152

Gamache, J. F. and Houze Jr, R. A.   1983   Water budget of a mesoscale convective system in the tropics. *J. Atmos. Sci.*, **40**, 1835–1850

Goldenberg, S. B., Houze Jr, R. A. and Churchill, D. D.   1990   Convective and stratiform components of a winter monsoon cloud cluster determined from geosynchonous infrared satellite data. *J. Meteorol. Soc. Japan*, **68**, 37–63

Griffith, C. G., Woodley, W. L., Grube, P. G., Martin, D. W., Stout, J. and Sikdar, D. N.   1978   Rain estimation from geosynchonous satellite imagery—visible and infrared studies. *Mon. Weather Rev.*, **106**, 1153–1171

Heymsfield, G. M. and Fulton, R.   1988   Comparison of high-altitude remote aircraft measurements with radar structure of an Oklahoma thunderstorm: Implications for precipitation estimation from space. *Mon. Weather Rev.*, **116**, 1157–1174

Houghton, H. G.   1968   On precipitation mechanisms and their artificial modification. *J. Appl. Meteorol.*, **7**, 851–859

Houze Jr, R. A.   1977   Structure and dynamics of a tropical squall-line system. *Mon. Weather Rev.*, **105**, 1540–1567

    1982   Cloud clusters and large-scale vertical motions in the tropics. *J. Meteorol. Soc. Japan*, **60**, 396–410

    1989   Observed structure of mesoscale convective systems and implications for large-scale heating. *Q. J. R. Meteorol. Soc.*, **115**, 425–461

    1993   *Cloud dynamics.* Academic Press, San Diego

Houze Jr, R. A. and Cheng, C.-P.   1977   Radar characteristics of tropical convection observed during GATE: Mean properties and trends over the summer season. *Mon. Weather Rev.*, **105**, 964–980

Houze Jr, R. A. and Rappaport, E. N.   1984   Air motions and precipitation structure of an early summer squall line over the eastern tropical Atlantic. *J. Atmos. Sci.*, **41**, 553–574

Houze Jr, R. A. and Wei, T.   1987   The GATE squall line of 9–10 August 1974. *Adv. Atmos. Sci.*, **4**, 85–92

Kingsmill, D. E. and Houze Jr, R. A.   1995   'Aircraft observations of the interaction between convective clouds, the atmospheric boundary layer, and the ocean surface'. XXI General Assembly of the International Association for the Physical Sciences of the Oceans. Honolulu, HI

Leary, C. A.   1984   Precipitation structure of the cloud clusters in a tropical easterly wave. *Mon. Weather Rev.*, **112**, 313–325

Lilly, D. K.   1988   Cirrus outflow dynamics. *J. Atmos. Sci.*, **45**, 1594–1605

Lin, X. and Johnson, R. H.   1997   Kinematic and thermodynamic characteristics of the flow over the western Pacific warm pool during TOGA COARE. *J. Atmos. Sci.*, **53**, 695–715

Locatelli, J. D. and Hobbs, P. V.   1974   Fallspeeds and masses of solid precipitation particles. *J. Geophys. Res.*, **79**, 2185–2197

Lorenz, E. N.   1993   *The essence of chaos.* University of Washington Press, Seattle, USA

Lovejoy, S. and Austin, G. L.   1979   The sources of error in rain amount estimating schemes from GOES visible and IR satellite data. *Mon. Weather Rev.*, **107**, 1048–1054

Maddox, R. A., Howard, K. W., Bartels, D. L. and Rodgers, D. M.   1986   Mesoscale convective complexes in middle latitudes. Pp. 390–413 in *Mesoscale meteorology and forecasting.* Ed. P. Ray. American Meteorological Society

Mapes, B. E.   1993   Gregarious tropical convection. *J. Atmos. Sci.*, **50**, 2026–2037
                                      1997   The large-scale part of tropical mesoscale convective system circulations: A linear vertical spectral band model. *J. Meteorol. Soc. Japan.* (In Press)

Mapes, B. E. and Houze Jr, R. A.   1992   'Satellite-observed cloud clusters in the TOGA COARE domain'. *TOGA Notes.* 5–7 April
                                      1993   Cloud clusters and superclusters over the oceanic warm pool. *Mon. Weather Rev.*, **121**, 1398–2037
                                      1995   Diabatic divergence profiles in western Pacific mesoscale convective systems. *J. Atmos. Sci.*, **52**, 1807–1828

Meteorological Satellite Center   1989   'The GMS user's guide. Second edition'. (Available from the Meteorological Satellite Center, Tokyo, Japan.)

Murakami, M.   1983   Analysis of deep convective activity over the western Pacific and southeast Asia. Part I: Diurnal variation. *J. Meteorol. Soc. Japan*, **61**, 60–75

Nakazawa, T.   1988   Tropical super clusters within intraseasonal variations over the western Pacific. *J. Meteorol. Soc. Japan*, **66**, 823–839
                                      1995   Intraseasonal oscillations during the TOGA-COARE IOP. *J. Atmos. Sci.*, **73**, 305–319

Packard, N. H., Crutchfield, J. P., Farmer, J. D. and Shaw, R. S.   1980   Geometry from a time series. *Phys. Rev. Lett.*, **45**, 712–716

Pandya, R. E. and Durran, D. R.   1996   The influence of convectively generated thermal forcing on the mesoscale circulation around squall lines. *J. Atmos. Sci.*, **53**, 2924–2951

Raymond, D. J.   1994   Convective processes and tropical atmospheric circulations. *Q. J. R. Meteorol. Soc.*, **120**, 1431–1455
                                      1995   Regulation of moist convection over the west Pacific warm pool. *J. Atmos. Sci.*, **52**, 3945–3959

Raymond, D. J. and Blyth, A. M.   1986   A stochastic mixing model for nonprecipitating cumulus clouds. *J. Atmos. Sci.*, **43**, 2708–2718
                                      1989   Precipitation development in a New Mexico thunderstorm. *Q. J. R. Meteorol. Soc.*, **115**, 1397–1423

Roberts, R. E., Selby, J. E. and Biberman, L. M.   1976   Infrared continuum absorption by atmospheric water vapor in the 8–12 μm window. *Appl. Optics*, **15**, 2085–2090

Steiner, M., Houze Jr, R. A. and Yuter, S. E.   1995   Climatological characterization of three-dimensional storm structure from operational radar and rain gauge data. *J. Appl. Meteorol.*, **34**, 1978–2007

Stephens, G. L.   1994   *Remote sensing of the lower atmosphere: An introduction.* Oxford University Press, New York

Wallace, J. M. and Hobbs, P. V.   1977   *Atmospheric science: An introductory survey.* Academic Press, New York

Webster, P. J. and Lukas, R.   1992   TOGA COARE: The coupled ocean–atmosphere response experiment. *Bull. Am. Meteorol. Soc.*, **73**, 1377–1416

Williams, M. and Houze Jr, R. A.   1987   Satellite-observed characteristics of winter monsoon cloud clusters. *Mon. Weather Rev.*, **115**, 505–519

Wu, R., Weinman, J. A. and Chin, R. T.   1985   Determination of rainfall rates from GOES satellite images by a pattern recognition technique. *J. Atmos. Oceanic Technol.*, **2**, 314–330

Yang, M.-J. and Houze Jr, R. A.   1996   Momentum budget of a squall line with trailing stratiform precipitation: Calculations from a high-resolution numerical model. *J. Atmos. Sci.*, **53**, 3629–3652

Yuter, S. E. and Houze Jr, R. A.　　1995a　Three-dimensional kinematic and microphysical evolution of Florida cumulonimbus. Part II: Frequency distributions of vertical velocity, reflectivity, and differential reflectivity. *Mon. Weather Rev.*, **123,** 1941–1963

1995b　Three-dimensional kinematic and microphysical evolution of Florida cumulonimbus. Part III: Vertical mass transport, mass divergence, and synthesis. *Mon. Weather Rev.*, **123,** 1964–1983

1997　Western Pacific warm pool region reflectivity rain rate relation derived from aircraft drop-size distribution data. *J. Appl. Meteorol.*, (In Press)

Yuter, S. E., Houze Jr, R. A., Smull, B. F., Marks Jr, F. D., Daugherty, J. R. and Brodzik, S. R.　　1995　TOGA COARE aircraft mission summary images: An electronic atlas. *Bull. Am. Meteorol. Soc.*, **76,** 319–328

Zhang, C.　　1996　Atmospheric intraseasonal variability at the surface in the tropical western Pacific Ocean. *J. Atmos. Sci.*, **53,** 739–758

Zipser, E. J.　　1988　The evolution of mesoscale convective systems: Evidence from radar and satellite observations. Pp. 159–166 in *Tropical rainfall measurements.* Eds. J. S. Theon and N. Fugono. Deepak Publishing